



UvA-DARE (Digital Academic Repository)

Ferrocene-based light-responsive carbon nano hoops

Kręcijasz, R.B.

Publication date
2026

[Link to publication](#)

Citation for published version (APA):

Kręcijasz, R. B. (2026). *Ferrocene-based light-responsive carbon nano hoops*. [Thesis, fully internal, Universiteit van Amsterdam].

General rights

It is not permitted to download or to forward/distribute the text or part of it without the consent of the author(s) and/or copyright holder(s), other than for strictly personal, individual use, unless the work is under an open content license (like Creative Commons).

Disclaimer/Complaints regulations

If you believe that digital publication of certain material infringes any of your rights or (privacy) interests, please let the Library know, stating your reasons. In case of a legitimate complaint, the Library will make the material inaccessible and/or remove it from the website. Please Ask the Library: <https://uba.uva.nl/en/contact>, or a letter to: Library of the University of Amsterdam, Secretariat, P.O. Box 19185, 1000 GD Amsterdam, The Netherlands. You will be contacted as soon as possible.

3

Strain-Induced Photochemical Opening of
Ferrocene[6]cycloparaphenylene:
Uncaging of Fe^{2+} with Green Light

Abstract

We present the synthesis, structural analysis and remarkable reactivity of the first carbon nanohoop that fully incorporates ferrocene in the macrocyclic backbone. The high strain imposed on the ferrocene by the curved nanohoop structure enables unprecedented photochemical reactivity of this otherwise photochemically inert metallocene complex. Visible light activation triggers a ring-opening of the nanohoop structure fully dissociating the Fe–cyclopentadienyl bonds in the presence of 1,10-phenanthroline. This process uncages Fe²⁺ ions captured in the form of [Fe(phen)₃]²⁺ complex in high chemical yield and can operate efficiently in a water-rich solvent with green light excitation. The measured quantum yields of [Fe(phen)₃]²⁺ formation show that embedding ferrocene into a strained nanohoop boosts its photoreactivity by three orders of magnitude compared to an unstrained ferrocene macrocycle or ferrocene itself. Our data suggest that the dissociation occurs by intercepting the photoexcited triplet state of the nanohoop by the nucleophilic solvent or external ligand. The strategy portrayed in this work proposes that new, tunable reactivity of analogous metallamacrocycles can be achieved with spatial and temporal control, which will aid and abet development of responsive materials for metal ions delivery and supramolecular, organometallic, or polymer chemistry.

The content of this chapter has been published as: **R. B. Křečijasz**, J. Malinčík, S. Mathew, P. Štacko, T. Šolomek. Strain-Induced Photochemical Opening of Ferrocene[6]cycloparaphenylene: Uncaging of Fe²⁺ with Green Light. *J. Am. Chem. Soc.* **2025**, *147*, 10231–10237.

3.1 Introduction

Iron is the single most important transition metal in the human body. While primarily renowned for its role in oxygen transport and storage within hemoglobin and myoglobin,^[1] iron fulfills numerous other critical roles in biological systems.^[2] Iron is a crucial component of cytochromes involved in the energy-providing electron transport chain in mitochondria.^[3] Ribonucleotide reductase—an iron-dependent enzyme—is necessary in the synthesis of deoxyribonucleotides, the building blocks of DNA that are crucial for cell division and repair.^[4] Iron also acts as a co-factor for various enzymes responsible for protection from oxidative stress^[5,6] or in the synthesis/degradation of hormones and neurotransmitters.^[7–9] Nature has developed a sophisticated system to tightly regulate iron's uptake and homeostasis through proteins and hormones like transferrin, ferroportin, ferritin and hepcidin.^[10] This system ensures a delicate balance between meeting physiological iron needs and preventing the adverse effects of iron overload. For instance, iron levels are reduced to restrict its availability to pathogens in response to inflammation, but this action can also impair immune cell function.^[11–13] Artificial systems that mimic these functions or exert spatiotemporal control over iron levels are consequently attractive in the context of potential biomedical applications.

Ferrocene (**Fc**) with its captivating sandwich structure featuring a central iron atom represents one of the most studied organometallic compounds since its discovery in the early 1950s.^[14] Its popularity can be attributed to a unique combination of its redox chemistry, structural fluxionality, and exceptional chemical and photochemical stability that parallels aromatic compounds. In fact, the iron-cyclopentadienyl (Fe–Cp) bond dissociation energy (BDE) of ~ 90 kcal mol⁻¹ is similar to that of a typical covalent C–C bond.^[15] As a result, the excellent redox properties and robustness made this metallocene class of materials particularly attractive for diverse applications that span polymer science,^[16,17] sensing,^[18,19] catalysis,^[18,20] biochemistry,^[21] and molecular electronics.^[18,22]

Imparting strain to **Fc** increases the propensity of this otherwise inert compound to undergo a cleavage of the Fe–Cp bond. This has been successfully exploited in a light-induced ring-opening polymerization (ROP) via Fe–Cp bond dissociation in strained [*n*]ferrocenophanes ($E_{\text{strain}} = 14\text{--}31$ kcal mol⁻¹).^[16,23–27] In these molecules, the two Cp rings are bridged via a few atoms ($n = 1\text{--}2$, Figure 3.1a) linked with single bonds. Although diverse polymers can be achieved via substitution of the bridging atoms or the Fc core itself, the linkers must be short and they interrupt the π -conjugation in the polymer. Recently, polymers with **Fc** incorporated in their backbone were shown to be susceptible to mechanically triggered Fe–Cp bond scission (Figure 3.1b), eventually releasing Fe²⁺ or Fe³⁺ ions.^[28–30] Here, [*n*]ferrocenophanes ($n = 3, 5$) were also used to tune the mechanical sensitivity of the Fc mechanophore.^[30]

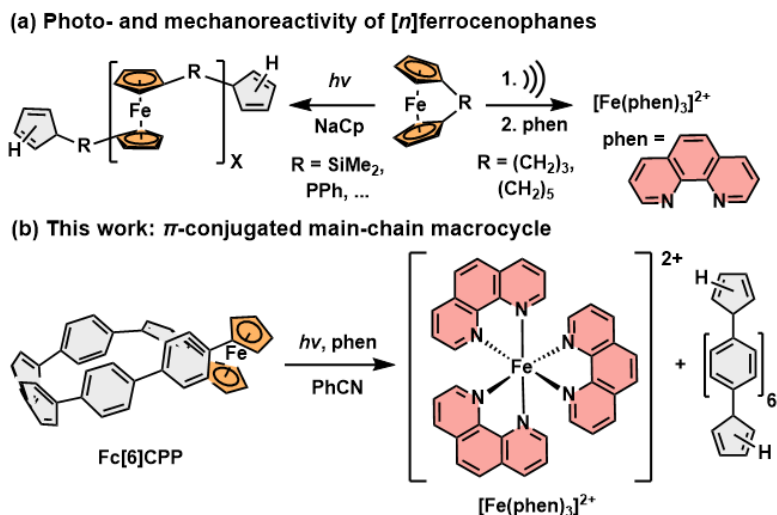


Figure 3.1. (a) Examples of photo-^[16,23–27] and mechanoactive^[28–30] $[n]$ ferrocenophanes, and (b) conceptually new photoactive ferrocene-based π -conjugated macrocycle described in this work.

Achieving the iron release on demand using a benign light activation would represent a great tool to control the concentration of available iron in a sample. However, such accomplishment would require developing robust methods to tune the strain in the Fc unit to control its reactivity. Cycloparaphenylenes (CPPs)^[31,32] are a unique class of highly strained, curved π -conjugated macrocycles consisting solely of phenylene rings connected through *para* positions. CPPs and related carbon-rich molecular systems, so-called carbon nano hoops, can be modified to alter the molecular strain and curvature by manipulating the number of *para*-phenylene units in the macrocycle. Therefore, CPP scaffold offers an elegant way to control the structural strain of a unit incorporated in the corresponding carbon nano hoop. We hypothesized that embedding **Fc** into a highly-strained, fully π -conjugated macrocycle^[33,34] such as CPP via both Cp rings could represent the robust strategy to impose the strain on **Fc**, enabling the control of **Fc** reactivity. The resultant conjugated, shape-persistent metallocene carbon nano hoops could lead to new applications demanding light- and force-sensitive materials. Although a handful of organometallic compounds based on the CPP scaffold have been reported, the metal atom in these structures is not an integral part of the macrocyclic backbone and it is therefore subject to a lower amount of strain than what the curved CPP structures could provide.^[33–38]

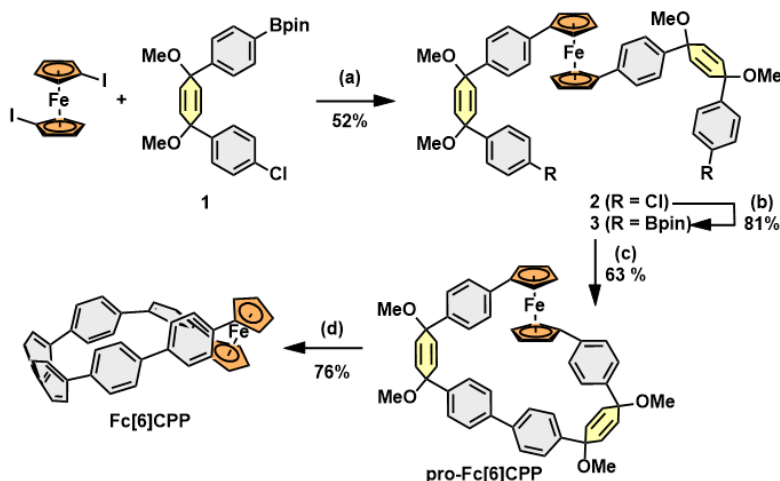
Here, we report the synthesis and properties of the first ferrocene-cycloparaphenylene **Fc** $[n]$ **CPP** ($n = 6$) with Fc enclosed in a loop of six *para*-phenylene rings. The considerable strain imparted on the Fc unit in **Fc** $[6]$ **CPP** enables its unprecedented photoreactivity that allows to open the nano hoop structure and release Fe^{2+} in high yield at ambient conditions using benign blue or green light in polar solvents (Figure 3.1b). The nano hoop **Fc** $[6]$ **CPP** thus serves as a

photoactivatable molecular storage system of Fe^{2+} ions, reminiscent of ferritine, but with a deliberate spatiotemporal control.

3.2 Results and Discussion

Fc[6]CPP was prepared in four steps (Scheme 3.1) from the reported 1,1'-diiodoferrocene and building block **1** following the methodology developed by Jasti.^[31] First, the Suzuki cross-coupling of 1,1'-diiodoferrocene with **1** provided intermediate **2** in 52% yield. The chlorides in intermediate **2** were then replaced by Miyaura borylation forming diboronate **3** in 81% yield. Subsequently, the intramolecular oxidative homocoupling^[39] of **3** afforded the pro-aromatic macrocycle **pro-Fc[6]CPP** in a very good 63% yield. The reductive aromatization of the two cyclohexa-2,5-dienyl units in **pro-Fc[6]CPP** using SnCl_2/HCl ^[40] proceeded smoothly and a pure sample of **Fc[6]CPP** could be isolated avoiding column chromatography in 76% yield. The final nano-hoop **Fc[6]CPP** is soluble in dichloromethane and THF and displays high chemical stability when stored at ambient conditions over a few months as a solid. The structures of both macrocycles **pro-Fc[6]CPP** and **Fc[6]CPP** were confirmed by 1D and 2D NMR spectroscopy and high-resolution mass spectrometry.

Single crystals were obtained by a vapor diffusion of *n*-hexane into a toluene solution (20 °C) of **pro-Fc[6]CPP** and by a vapor diffusion of methanol into a THF solution (at 4 °C) of **Fc[6]CPP**.



Scheme 3.1. Synthesis of **Fc[6]CPP**. Reaction conditions: (a) **1** (3 equiv.), $\text{Pd}(\text{dppf})\text{Cl}_2$ (0.05 equiv.), NaOH (4 equiv.), $\text{DME}/\text{H}_2\text{O}$, 85 °C, 20 h (b) B_2pin_2 (4 equiv.), $\text{Pd}_2(\text{dba})_3$ (0.05 equiv.), XPhos (0.2 equiv.), KOAc (8 equiv.), 1,4-dioxane, 110 °C, 16 h (c) $\text{Pd}(\text{dppf})\text{Cl}_2$ (0.1 equiv.), KF (1 eq.), $\text{B}(\text{OH})_3$ (5 equiv.), $\text{THF}/\text{H}_2\text{O}$, air, 40 °C, 20 h (d) H_2SnCl_4 (3.6 equiv.), THF , RT, 2 h.

The X-ray diffraction analysis unequivocally confirmed their macrocyclic structure (Figure 3.2). Compound **pro-Fc[6]CPP** crystallized in triclinic $P\bar{1}$ space group and Fc fluxionality allowed it to adopt a triangular shape. Both enantiomers with opposite helicity (Figures S3.2–S3.3) can be clearly distinguished in the crystal. Nanohoop **Fc[6]CPP** crystallized in monoclinic $P2_1$ space group. Here, the Fc flexibility allowed the macrocycle to adopt an oval shape (Figure 3.2b) typical for *meta*-CPPs^[41] and related nanohoops.^[42,43] The size of the elliptic cavity is 12.6 Å in length and 7.0 Å in width. The connecting Cp carbon atoms in Fc moiety are nearly eclipsed. Further analysis of the crystal structures revealed the effect of the strain imparted onto Fc by the curvature of the macrocycles. The tilt angle α defined by the planes of the Cp rings and the Cp–Fe–Cp angle δ —common descriptors describing ferrocenophanes (see Figure S3.1)—differ in **pro-Fc[6]CPP** (Table S3.2) from the ideal values^[44] in unstrained **Fc** ($\alpha = 0^\circ$; $\delta = 180^\circ$) only slightly. On the other hand, the values determined for **Fc[6]CPP** (10.62° ; 172.84°) clearly indicate that part of the total strain in the macrocycle has been transferred to Fc. The deviation from the ideal angles correlates with E_{strain} of 13.7 and 82.6 kcal mol⁻¹ calculated for both **pro-Fc[6]CPP** and **Fc[6]CPP**, respectively, using homodesmotic reactions (Scheme S3.1). The DFT-calculated geometries reproduce the crystal structures well and the calculated strain in **Fc[6]CPP** approaches that of [7]CPP ($E_{\text{strain}} = 84.0$ kcal mol⁻¹).^[45] Despite the significant strain, the Fc in **Fc[6]CPP** is markedly less distorted than less strained [1]- and [2]ferrocenophanes (14–31 kcal mol⁻¹; $\alpha = 19\text{--}31^\circ$ and $\delta = 156\text{--}167^\circ$).^[25,46–48] Although, the strain energies in [n]ferrocenophanes and **Fc[6]CPP** markedly differ, the strain calculated per atom is comparable, which highlights its

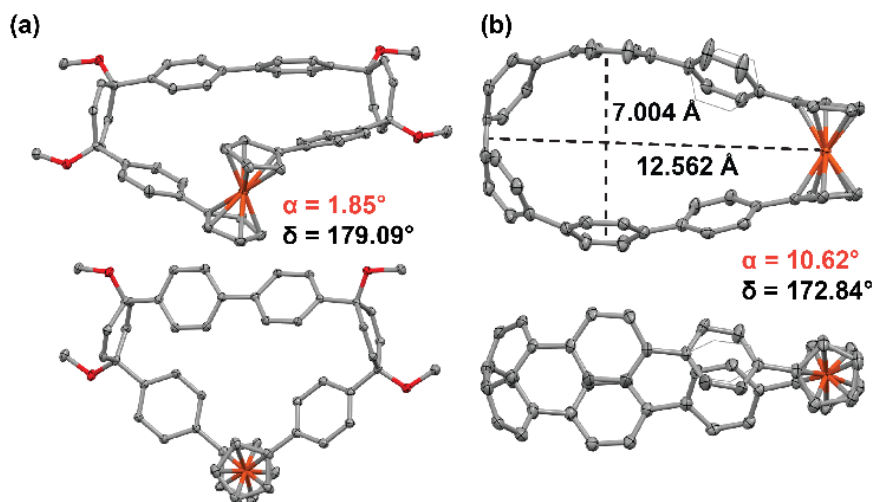


Figure 3.2. X-ray crystal structures of (a) **pro-Fc[6]CPP** (selected conformer, see Appendix) and (b) **Fc[6]CPP** (thermal ellipsoids shown at 50% probability; all hydrogen atoms and solvent were omitted for clarity). Gray: C, red: O, orange: Fe. The carbon atoms of one phenyl group in (b) are disordered over two sites with relative occupancies of 0.602:0.398.

different distribution. The values of α and δ suggest that Fc in **Fc[6]CPP** is less strained than the known $[\eta]$ ferrocenophanes. The large distortion of Fc moiety in the latter compounds is known to weaken the Fe–Cp bond and to induce its cleavage upon irradiation. However, the Fc distortion observed for **Fc[6]CPP** matches that found in $\text{Fe}(\eta\text{-C}_5\text{H}_4)_2(\text{CHCHCHCH})$ (10.2° ; 173.08°),^[49] a compound known to be stable in air as a solid and in a solution,^[50] for which no photolytic processes are reported in the literature.

We examined if embedding a Fc unit into a strained macrocyclic structure affected the optical and redox properties. The latter were determined for CH_2Cl_2 solutions of **Fc[6]CPP** with 0.1 M $[\text{n-Bu}_4\text{N}][\text{PF}_6]$ as a supporting electrolyte using cyclic voltammetry (CV) and differential pulse voltammetry (DPV). A single anodic wave could be observed for **Fc[6]CPP** (Figures S3.7–S3.8) with only a minor shift in the half-wave oxidation potential ($E_{1/2}$) by ca -50 mV with respect to the Fc/Fc⁺ couple. The Randles–Ševčík analysis revealed a full reversibility of the oxidation process at the electrode (Figure S3.9). We then recorded the absorption spectra of **Fc[6]CPP** and **pro-Fc[6]CPP** (Figure 3.3, Table 3.1). Nano hoop **Fc[6]CPP** exhibits a characteristic absorption profile observed for $[\eta]$ CPPs with an intense transition at 330 nm ($\epsilon = 5.2 \times 10^4 \text{ M}^{-1} \text{ cm}^{-1}$) and a distinct band at ~ 400 nm, which corresponds to the $S_0 \rightarrow S_1$ transition in CPPs. A weak solvatochromism is observed for **Fc[6]CPP** (Figure S3.10). Comparison to the absorption spectrum of **pro-Fc[6]CPP**, in which the conjugation in the macrocycle is interrupted by the pro-aromatic cyclohexa-2,5-dienyls, suggests that an unresolved low-energy transition (>450 nm) may exist in **Fc[6]CPP**. This is supported by TD–DFT calculations that predict that nearly-degenerate Fc-centered transitions with a low oscillatory strength represent the lowest excited states in

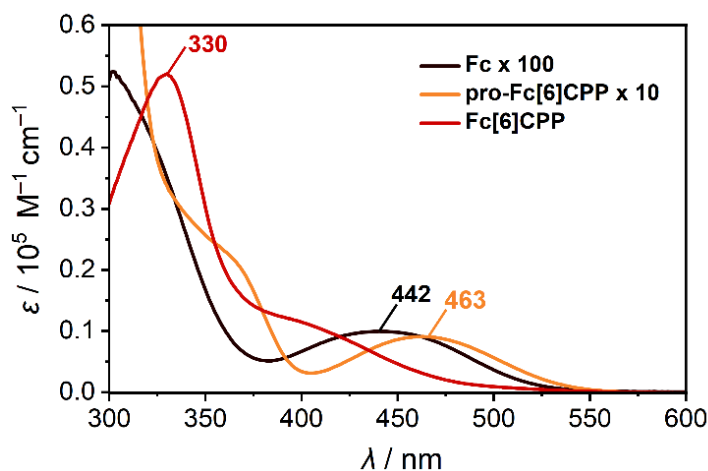


Figure 3.3. UV–vis absorption spectra of **Fc**, **pro-Fc[6]CPP** and **Fc[6]CPP** in PhCN. For the sake of comparison, the spectra of **Fc** and **pro-Fc[6]CPP** were scaled by a factor of 100 and 10, respectively.

Fc[6]CPP. Indeed, such $d-d$ transitions are clearly visible at 442 nm ($\epsilon = 90 \text{ M}^{-1} \text{ cm}^{-1}$) in **Fc**.^[51,52] Their slight bathochromic shift with the corresponding increase of ϵ in **Fc[6]CPP** is the consequence of extending the π -system of the Cp ligands and decreasing the overall symmetry of the chromophore, partially allowing the $d-d$ transitions as shown by the natural transition orbitals analysis of the first seven transitions in **Fc[6]CPP** (see Appendix). Despite the presence of the curved *para*-phenylene segment, **Fc[6]CPP** displays no luminescence. This confirms that the lowest-energy excited state in both **pro-Fc[6]CPP** and **Fc[6]CPP** is localized on the Fc moiety, a known luminescence quencher.

Interestingly, while the absorption spectrum of **Fc[6]CPP** in toluene ($c \approx 20 \mu\text{M}$) did not change upon exposure to ambient light (96 hours, Figure S3.11), an equally concentrated sample of **Fc[6]CPP** in polar PhCN displayed a notable change in color within dozens of minutes. The photolysis rate is rapid when green light ($\lambda_{\text{LED}} = 525 \pm 18 \text{ nm}$, $>10 \text{ mW}$) is used as the light source and the characteristic CPP band at 330 nm is no longer discernible after 30 min of irradiation (Figure S3.12). Note that **Fc[6]CPP** remains stable in the dark for $>24 \text{ h}$ at room temperature (Figure 3.4a). Similar experiments with samples of **pro-Fc[6]CPP** or **Fc** revealed a striking difference among the compounds. Both **pro-Fc[6]CPP** and **Fc** in PhCN are stable over days when exposed to daylight (Figures S3.13–S3.14). Based on the known cases of Fe–Cp bond dissociation triggered by irradiation^[16,23–27] or mechanical force,^[28–30] we hypothesized that **Fc[6]CPP** might undergo a macrocyclic ring opening, eventually releasing the Fe^{2+} ion and the substituted *p*-sexiphenyl (Figure 3.1b). To test this hypothesis, the solution of **Fc[6]CPP** was exposed to ambient light in presence of 500 equiv. of 1,10-phenanthroline (phen), which is known to bind Fe^{2+} ion to form ferriox, $[\text{Fe}(\text{phen})_3]^{2+}$ complex with a distinct absorption spectrum. After 24 h, the solution was filtered, and its absorption spectrum matched that of the independently

Table 3.3. Summary of photophysical, redox and structural properties.

Compd.	λ_{abs} (nm)	ϵ^a ($10^3 \text{ M}^{-1} \text{ cm}^{-1}$)	$E_{1/2}$ (mV)	E_{strain}^b (kcal mol ⁻¹)	Φ^c (%)
Fc	442	0.1	0.0	0.0	$(1.5 \pm 0.3) \times 10^{-3}$
pro-Fc[6]CPP	463	0.9	-	13.7	$(4.9 \pm 0.4) \times 10^{-3}$
Fc[6]CPP	330	52; 2.3 ^d	-42^e ; -57^f	82.6	6.0 ± 0.5

^a At maximum λ_{abs} . ^b At D3-B3LYP/6-31++g(d)/LanL2DZ(Fe) level of theory; see the SI for the computational details. ^c Absolute quantum yield of $[\text{Fe}(\text{phen})_3]^{2+}$ formation in PhCN with 500 equiv. of phen \pm standard deviation of the mean. ^d At $\lambda_{\text{abs}} = 472 \text{ nm}$. ^e Determined by CV. ^f Determined by DPV.

prepared sample of $[\text{Fe}(\text{phen})_3]^{2+}$ (Figure 3.4b). The nature of the complex was also confirmed by mass spectrometry (Figure S3.15). Besides the photoinduced release and subsequent catch of Fe^{2+} from the nano hoop, we observed formation of a precipitate that likely corresponds to the released *p*-sexiphenyl derivative. However, we have not yet been able to unequivocally identify the structure of the latter by mass spectrometry. We determined the yield of $[\text{Fe}(\text{phen})_3]^{2+}$ formation by absorption spectroscopy (see Appendix) to be $(80 \pm 3.0) \%$ and $(67 \pm 5.2) \%$ before and after filtration of the photolyzed solution, respectively. The difference stems from the presence of the precipitate, which leads to a slight scattering at the absorption band of $[\text{Fe}(\text{phen})_3]^{2+}$. The control experiments conducted at room temperature in dark with large excess of phen (500 equiv.) showed a minor $[\text{Fe}(\text{phen})_3]^{2+}$ formation ($<10 \%$ after 24 h, unfiltered, Figure S3.17). However, increasing the temperature to $70 \text{ }^\circ\text{C}$ resulted in a markedly faster transformation (Figure S3.18), although the reaction required a few days to reach a full conversion. These observations strongly support our assumption that the strain perturbing the Fc structure markedly affects the reactivity of Fc in **Fc[6]CPP**.

To quantify the reactivity of **Fc[6]CPP**, we compared its photochemical behaviour with the less strained precursor **pro-Fc[6]CPP** as well as the unstrained **Fc** itself. For this purpose, we measured the absolute quantum yields of $[\text{Fe}(\text{phen})_3]^{2+}$ formation in PhCN for all three compounds (Φ , Table 3.1) under identical conditions ($c = 40 \text{ } \mu\text{M}$, 500 equiv. of phen, $\lambda_{\text{LED}} = 472 \text{ nm}$). The large excess of phen was necessary to detect appreciable amount of $[\text{Fe}(\text{phen})_3]^{2+}$ formed from both **pro-Fc[6]CPP** and **Fc** within hours at the full intensity of our LED source (130 mW), while **Fc[6]CPP** could be converted in seconds. Comparison of the measured Φ 's reveals the striking enhancement of the reactivity of **Fc[6]CPP**. While the determined Φ 's for **Fc** and **pro-Fc[6]CPP** are $(1.5 \pm 0.3) \times 10^{-5}$ and $(4.9 \pm 0.4) \times 10^{-5}$, respectively, the ring-opening in **Fc[6]CPP**

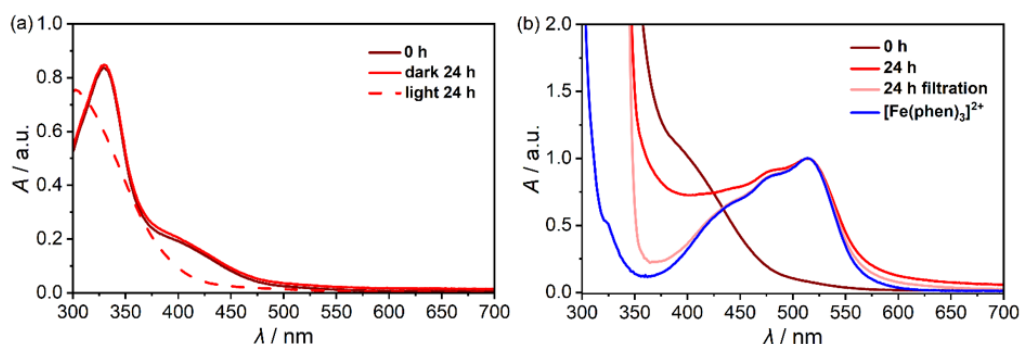


Figure 3.4. (a) **Fc[6]CPP** in PhCN ($c \approx 20 \text{ } \mu\text{M}$) stirred in dark (solid line) or in ambient light (dashed line) and (b) normalized absorption spectra of **Fc[6]CPP** in PhCN ($c \approx 60 \text{ } \mu\text{M}$, phen: 500 equiv.) stirred in ambient light for 24 h (red: unfiltered, light red: filtered) and independently prepared $[\text{Fe}(\text{phen})_3]^{2+}$ (blue). The spectrum at 0 h (dark red) was scaled to match the ϵ of $[\text{Fe}(\text{phen})_3]^{2+}$.

is >1'000-fold more efficient. The value of Φ reflects the Fc tilt angle and the strain energy in the individual compounds (Table 3.1), but it also depends strongly on the concentration of the phen ligand (Figure 3.5). The quantum yield for **Fc[6]CPP** grew from 1.6×10^{-3} to 0.06 with increasing amount of phen. The Φ levels off at large excess of phen and reaches a limiting value that compares favourably to the intersystem crossing quantum yield reported for **Fc** ($\Phi_{\text{ISC}} = 0.085$).^[53] It suggests that the Fe–Cp bond dissociation occurs by intercepting the excited Fc unit by a ligand molecule. This step may take place efficiently only in **³Fc** that possesses sufficiently long excited state lifetime ($\tau(^3\text{Fc}) = 90 \text{ ns}$ vs $\tau(^1\text{Fc}) = 10 \text{ ps}$).^[53] A simulation of the expected Φ of $[\text{Fe}(\text{phen})_3]^{2+}$ formation via a triplet state, while accounting for the quenching of the oxygen present in the solution matches the observed concentration dependence well (Figure 3.5). Comparison of the Φ 's determined in the presence and the absence of oxygen with 10 equiv of phen in the solution showed a statistically significant difference ($t(6)=2.26$, $p < 0.05$), confirming that the reaction occurs via the triplet state of **Fc[6]CPP**. Indeed, the DFT-calculated spin density shows an antibonding character of the Fe–Cp bond in triplet **Fc[6]CPP** and the presence of an electron hole at the Fe centre (Figure S3.35). This increases iron electrophilicity^[47,54] promoting the bond dissociation when attacked by a nucleophilic solvent or external ligand.^[16] Such polar transition state is in agreement with our observation that the photolysis of **Fc[6]CPP** is facile in polar PhCN (Figure 3.4a) and inefficient in toluene (Figure S3.11). It has also been reported that electron donating solvents promote the Fe–Cp bond dissociation.^[25,55–57] We thus expect that a half-sandwich complex **7** (Scheme 3.2) is formed as the first reaction step with temporarily coordinated solvent and the *p*-sexiphenyl ligand still attached to the Fe via the remaining Cp. Subsequently, excess phen must rapidly replace the labile ligands because we do not observe formation of any intermediates by UV–vis spectroscopy with 250 ms sampling. A complex such as **7** has been

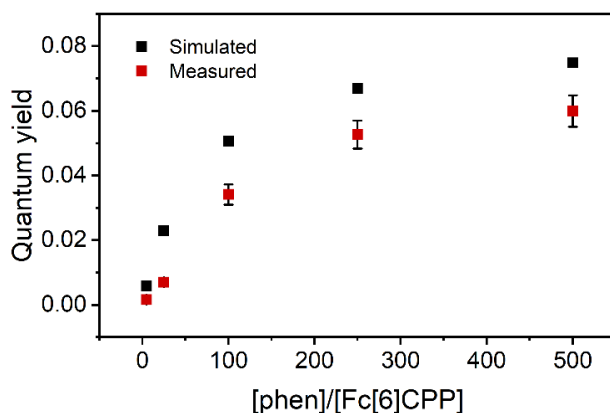
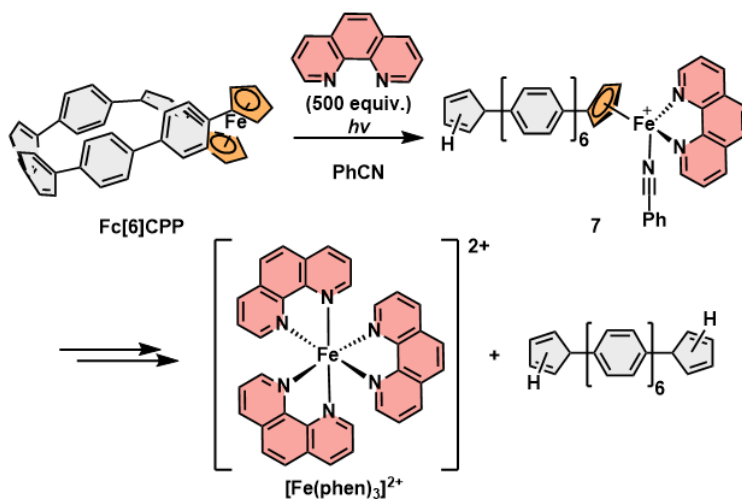


Figure 3.5. Measured (red, with standard deviation) and simulated (black, see the SI for details) quantum yields of $[\text{Fe}(\text{phen})_3]^{2+}$ formation from **Fc[6]CPP** in PhCN upon irradiation with 472 nm LED as a function of phen concentration.



Scheme 3.2. Proposed mechanism for dissociation in presence of phen of **Fc[6]CPP** upon irradiation.

often proposed^[58–60] as an intermediate in dissociation of [1]- and [2]ferrocenophanes, but it has never been detected. Note that no free Fe^{2+} forms directly from **Fc[6]CPP**, which we verified by photolysis of the **Fc[6]CPP** before an addition of phen (500 equiv.) to the PhCN solution. Here, we observed only a slow formation (>72 h) of $[\text{Fe(phen)}_3]^{2+}$ in dark. The process proceeded somewhat faster under ambient light. However, complexation of Fe(OTf)_2 in PhCN treated with excess phen occurs rapidly (<10 min, compare Figures S3.29–3.31).

As shown above, **Fc[6]CPP** undergoes a remarkably clean ring opening reaction in polar environment upon irradiation with benign light. The elevated strain energy of the nanohoop makes the photochemical Fe–Cp bond dissociation and subsequent Fe^{2+} release and trapping particularly efficient. Given the crucial role of iron in various biological processes, we decided to probe the photoreactivity of **Fc[6]CPP** in mixed aqueous/organic medium due to negligible solubility of the nanohoop in pure water. The irradiation of **Fc[6]CPP** in a mixture of $\text{H}_2\text{O/THF}$ ($v/v = 1:1$, 500 equiv. phen) with green light resulted in the formation of $[\text{Fe(phen)}_3]^{2+}$. Here, $[\text{Fe(phen)}_3]^{2+}$ formed cleanly in $(81 \pm 1.1)\%$ yield after filtration (Figure S3.33) with $\sim 75\%$ efficiency compared to the experiment in neat PhCN. The iron release from **Fc[6]CPP** upon irradiation is thus a highly effective process also in polar protic solvents, which creates exciting opportunities for biological applications such as delivery and dosing of iron controlled by light. It is important to note here that although the macrocyclic structure of **Fc[6]CPP** irreversibly opens upon irradiation without phen, the presence of phen alters the iron release mechanism and significantly enhances the overall release rate. The nature and the kinetic stability of the formed

primary complex in water in the absence of phen requires detailed mechanistic scrutiny to reveal how it might be decomposed to release iron using nucleophiles ubiquitous in biological system.

The tunability of strain in carbon nano hoops by precision synthesis may represent a great tool to uncover and control the reactivity in similar type of metallamacrocycles as the one designed in this work, which could aid the development of new redox-active or supramolecular systems that are responsive to light or mechanical force. Work along these lines is currently ongoing in our laboratories.

3.3 Conclusion

In summary, we synthesized a highly-strained π -conjugated macrocycle **Fc[6]CPP** that incorporates ferrocene. Its structure was unequivocally characterized by the X-ray diffraction analysis and quantum chemical calculations. The high strain in **Fc[6]CPP** transforms the reactivity of photostable ferrocene into a photoactivatable carrier of iron that is released via iron–cyclopentadienyl bond cleavage and easily trapped with phenanthroline to form ferriin complex. The observed clean and high-yielding reaction is three orders of magnitude more efficient than that for ferrocene and demonstrates the power of molecular strain to uncover and control reactivity of an otherwise stable metallocene complex. Furthermore, we demonstrated that this system efficiently releases iron in a mixed aqueous/organic environment, suggesting that its operation can be translated to biological context. We believe that this work will thus motivate new developments in the fields of responsive materials, photocages, or organometallic and host–guest chemistry.

3.4 Appendix

All commercially available reagents and chemicals were purchased from Sigma Aldrich, TCI, Fluorochem and Fisher Scientific and used as received without further purification, unless stated otherwise. Anhydrous solvents were purchased from Acros and stored under molecular sieves (4 Å). Technical solvents were bought from VWR International and Biosolve, and were used as received. Unless otherwise stated, all glassware used to perform moisture-sensitive reactions was oven-dried at 120 °C overnight, assembled hot and allowed to cool down to room temperature under a stream of argon, or flame-dried under high vacuum and filled with argon. All reactions that require heating were conducted in an oil bath and the indicated temperature corresponds to the temperature of the oil bath. Flash column chromatography was performed using silica gel 60 Å (230–400 mesh particle size) from Supelco®. Thin layer chromatography (TLC) was performed

on silica gel plates F₂₅₄ 60 (aluminum supported) from Supelco® using UV (254 nm) visualization. Recycling gel permeation chromatography (GPC) was performed on LaboAce 5060 preparative HPLC from Japan Analytical Services using Chloroform as the solvent. ¹H and ¹³C NMR spectra were recorded on a Bruker Avance II 400 or a Bruker Avance III HD 400 spectrometer (¹H: 400 MHz, ¹³C: 101 MHz), or Bruker Avance III HD 300 (¹H: 300 MHz, ¹³C: 75 MHz). Chemical shifts (δ) were reported in parts per million (ppm) referenced to residual solvent peak (¹H: 7.26 ppm for CDCl₃, 5.32 ppm for CD₂Cl₂; ¹³C: 77.16 ppm for CDCl₃, 53.84 ppm for CD₂Cl₂). Multiplicities are given as s (singlet), d (doublet), t (triplet), q (quadruplet), m (multiplet), and br (broad). Coupling constants (*J*) are reported in hertz (Hz). High resolution mass spectra (HRMS) were recorded on ThermoScientific LTQ Orbitrap XL mass instrument using nanoelectrospray (NSI-MS) or electron ionization (EI-MS) or on an AccuTOF LC, JMS-T100LP mass spectrometer (JEOL, Japan). UV-vis spectra were recorded with a double beam spectrophotometer Shimadzu UV2700 equipped with a deuterium lamp (190–350 nm), a halogen lamp (330–900 nm) and a photomultiplier (Hamamatsu R928). Single-crystal X-ray diffraction data measured on a Bruker D8 Quest Eco diffractometer using graphite-monochromated (Triumph) Mo K α radiation ($\lambda = 0.71073 \text{ \AA}$) and a CPAD Photon III C14 detector. The sample was cooled with N₂ to 100 K with a Cryostream 700 (Oxford Cryosystems).

3.4.1 Experimental procedures

1,1'-diiodoferrocene^[61] and **1**^[62] were prepared according to reported protocols.

Preparation of compound **2**

Compound **1** (3.10 g, 6.85 mmol, 3 equiv.) and NaOH (365 mg, 9.14 mmol, 4 equiv., CAS: 1310-73-2) were introduced in a Schlenk flask. The flask was evacuated and refilled with argon three times. Then, 1,1'-diiodoferrocene (1.00 g, 2.28 mmol, 1 equiv.) was added, followed by DME (30 mL) and water (6 mL). The mixture was purged with argon for 15 min, after which Pd(dppf)Cl₂ (84 mg, 0.114 mmol, 0.05 equiv., CAS: 72287-26-4) was added. The reaction mixture was stirred at 85 °C for 20 h, then allowed to cool down to room temperature, diluted with EtOAc (20 mL) and washed once with water (25 mL). The aqueous phase was extracted with EtOAc (3 × 15 mL). The combined organic layers were washed with brine, dried over Na₂SO₄ and concentrated in vacuo to afford a dark thick oil. The crude product was dissolved in a minimal amount of CH₂Cl₂ and an excess of MeOH was slowly added without disturbing the CH₂Cl₂ phase. The next day, the solution was filtered to give the pure product as the precipitate. Because the filtrate still contained some product, the purification with CH₂Cl₂/MeOH was repeated two more times. The repeated precipitations provided **2** as a brown solid (993 mg, 1.19 mmol, 52%).

Chapter 3

Brown solid; $R_f = 0.42$ (SiO₂, EtOAc: *n*-pentane = 1:4).

¹H NMR (300 MHz, CD₂Cl₂): $\delta = 7.45 - 7.10$ (m, 16H), 6.14 (d, $J = 10.3$ Hz, 4H), 6.04 (d, $J = 10.3$ Hz, 4H), 4.44 (t, $J = 1.9$ Hz, 4H), 4.18 (t, $J = 1.9$ Hz, 4H), 3.42 (s, 12H).

¹³C NMR (75 MHz, CD₂Cl₂): $\delta = 142.9, 141.4, 138.2, 134.3, 133.5, 133.3, 128.7, 128.0, 126.3, 126.3, 85.9, 75.0, 74.8, 71.3, 68.4, 52.2, 52.2$.

HRMS (ESI⁺): m/z [M]⁺ calcd for C₅₀H₄₄Cl₂O₄Fe: 834.1968; found: 834.1979.

Preparation of compound **3**

Compound **2** (779 mg, 0.932 mmol, 1 equiv.), bis(pinacolato)diboron (947 mg, 3.73 mmol, 4 equiv., CAS: 73183-34-3), Pd₂(dba)₃ (43 mg, 0.047 mmol, 0.05 equiv., CAS: 51364-51-3), XPhos (89 mg, 0.186 mmol, 0.2 equiv., CAS: 564483-18-7) and dry potassium acetate (732 mg, 7.46 mmol, 8 equiv., CAS: 127-08-2) were introduced to a Schlenk flask and purged with argon for 15 min. Anhydrous 1,4-dioxane (20 mL) purged with argon for 15 min was then added via cannula. The reaction mixture was stirred at 110 °C for 16 h. After the addition of water (25 mL), the reaction was extracted with CH₂Cl₂ (3 × 25 mL). The combined organic layers were washed with brine, dried over Na₂SO₄ and concentrated in vacuo to afford a brown solid. Crude product was washed several times with *n*-hexanes to afford **3** as brown solid (769 mg, 0.755 mmol, 81%).

Brown solid; $R_f = 0.33$ (SiO₂, EtOAc: *n*-pentane = 1:4).

¹H NMR (300 MHz, CDCl₃): $\delta = 7.78$ (d, $J = 7.8$ Hz, 4H), 7.44 (d, $J = 7.8$ Hz, 4H), 7.35 – 7.20 (m, 8H), 6.23 – 6.00 (m, 8H), 4.48 (t, $J = 1.9$ Hz, 4H), 4.15 (t, $J = 1.9$ Hz, 4H), 3.45 (s, 12H), 1.34 (s, 24H).

¹³C NMR (75 MHz, CDCl₃): $\delta = 146.7, 141.0, 138.1, 135.0, 133.6, 133.2, 126.2, 126.1, 125.5, 85.7, 83.9, 75.1, 74.9, 71.2, 68.0, 52.1, 52.1, 25.0$, C-B signal not observed.

HRMS (NSI): m/z [M]⁺ calcd for C₆₂H₆₈O₈ B₂Fe: 1018.4444; found: 1018.4418.

Preparation of **pro-Fc[6]CPP**

We modified a literature procedure:^[39] To the solution of compound **3** (299 mg, 0.294 mmol, 1 equiv.) in THF (300 mL) were added Pd(dppf)Cl₂ (20 mg, 0.03 mmol, 0.1 equiv., CAS: 72287-26-4) and boric acid (91 mg, 1.470 mmol, 5 equiv., 10043-35-3). The reaction mixture was heated to 40 °C and meanwhile it was purged with oxygen for 10 min. Potassium fluoride (17 mg, 0.294 mmol, 1 equiv., CAS: 7789-23-3) in water (30 mL) was added. The reaction was stirred at 40 °C open to air for 20 h. The THF was removed in vacuo and the resulting solution was extracted with CH₂Cl₂ (3 × 20 mL). The combined organic layers were washed with water (2 × 25 mL), dried

over Na₂SO₄ and concentrated in vacuo to afford a brown solid. Crude product was purified by flash chromatography (SiO₂, EtOAc: *n*-pentane = 1:9 → EtOAc: *n*-pentane = 3:7) to afford **pro-Fc[6]CPP** as orange solid (125 mg, 0.163 mmol, 56 %). The impure fractions were further purified by GPC to afford the pure macrocycle (17 mg, 0.022 mmol, 7%, total yield = 63%).

Orange solid; *R_f* = 0.26 (SiO₂, EtOAc: *n*-pentane = 1:4).

¹H NMR (400 MHz, CDCl₃): δ = 7.51 (d, *J* = 8.5 Hz, 4H), 7.37 (d, *J* = 8.5 Hz, 4H), 7.28 (d, *J* = 8.5 Hz, 4H), 7.01 (d, *J* = 8.5 Hz, 4H), 6.33 – 6.28 (m, 4H), 6.21 – 6.18 (m, 2H), 6.12 – 6.09 (m, 2H), 4.37 (s, 2H), 4.29 (s, 2H), 4.03 (s, 2H), 3.98 (s, 2H), 3.41 (s, 6H), 3.36 (s, 6H).

¹³C NMR (101 MHz, CDCl₃): 141.3, 140.4, 139.7, 138.2, 133.8, 133.6, 133.6, 133.3, 127.4, 127.1, 126.8, 125.6, 86.7, 76.0, 75.9, 71.0, 70.9, 70.5, 64.9, 52.4, 52.1.

HRMS (NSI): *m/z* [M]⁺ calcd for C₅₀H₄₄O₄Fe: 764.2584; found: 764.2601.

Preparation of **Fc[6]CPP**

A 0.08 M H₂SnCl₄ solution was prepared by stirring SnCl₂·2H₂O (90.2 mg, 0.4 mmol, CAS: 10025-69-1) and concentrated HCl (12 M) (67 μL, 0.8 mmol, CAS: 7647-01-0) in THF (5 mL) at room temperature for 30 min. After this time, H₂SnCl₄ solution (0.08 M, 3.5 mL, 0.282 mmol, 3.6 equiv.) was added to **pro-Fc[6]CPP** (60.0 mg, 0.079 mmol, 1 equiv.) and the reaction was stirred at room temperature for 2 h. The reaction was quenched with 1 M NaOH (2 mL) and the aqueous layer was extracted with CH₂Cl₂ (3 × 10 mL). The organic layers were washed with brine, dried over Na₂SO₄ and concentrated in vacuo to afford **Fc[6]CPP** as dark red solid (38.4 mg, 0.060 mmol, 76%).

Dark red solid; *R_f* = 0.38 (SiO₂, EtOAc: *n*-pentane = 1:4).

¹H NMR (300 MHz, CDCl₃): δ = 7.50 – 7.43 (m, 12), 7.40 (d, *J* = 8.8 Hz, 4H), 7.24 (d, *J* = 8.5 Hz, 4H), 7.18 (d, *J* = 8.4 Hz, 4H), 4.37 (t, *J* = 1.8 Hz, 4H), 4.20 (t, *J* = 1.9 Hz, 4H).

¹³C NMR (75 MHz, CDCl₃): δ = 138.8, 138.7, 138.3, 137.8, 137.4, 136.8, 128.7, 128.3, 127.9, 127.9, 127.7, 127.3, 90.4, 69.9, 68.0.

HRMS (NSI): *m/z* [M]⁺ calcd for C₄₆H₃₂Fe: 640.1848; found: 640.1868.

3.4.2 Single crystal X-ray diffraction

X-ray diffraction data of **pro-Fc[6]CPP** and **Fc[6]CPP** were measured on a Bruker D8 Quest Eco diffractometer using graphite-monochromated (Triumph) Mo Kα radiation (*l* = 0.71073 Å) and a CPAD Photon III C14 detector. The sample was cooled with N₂ to 100 K with a Cryostream 700

(Oxford Cryosystems). Intensity data were integrated using the SAINT software.^[63] Absorption correction and scaling was executed with SADABS.^[64] The structures were solved using intrinsic phasing with the program SHELXT 2018/2^[65] against F2 of all reflections.

The crystal structure contained two voids (total solvent accessible volume = 144 Å³), containing THF solvent within the asymmetric unit could not be refined reliably. Thus, the SQUEEZE^[66] procedure in PLATON^[67] (version 141123) was applied, accounting for 38 electrons per unit cell, congruent with the presence of 1 THF molecule (40 e⁻/molecule) in the unit cell (Z=2).

Least-squares refinement was performed with SHELXL-2018/3.^[68] All non-hydrogen atoms were refined with anisotropic displacement parameters. The hydrogen atoms were introduced at calculated positions with a riding model. CheckCIF revealed no A- or B-level alerts. The X-ray crystallographic data for **pro-Fc[6]CPP** (2373507) and **Fc[6]CPP** (2373508) was deposited at the Cambridge Crystallographic Data Centre (CCDC).

Table S3.1. Crystallographic data and structure refinement details for **pro-Fc[6]CPP** and **Fc[6]CPP**.

CCDC number	2373507	2373508
Empirical formula	C _{54.56} H ₅₀ FeO ₄	C ₄₈ H ₃₆ FeO _{0.50}
Formula weight	825.51	676.62
Temperature [K]	100(2)	100(2)
Crystal system	triclinic	monoclinic
Space group (number)	<i>P</i> $\bar{1}$ (2)	<i>P</i> 2 ₁ (4)
a [Å]	12.1840(9)	11.5096(6)
b [Å]	20.5519(16)	10.3463(5)
c [Å]	27.401(2)	14.0369(7)
α [°]	75.872(3)	90
β [°]	85.312(3)	95.431(2)
γ [°]	73.239(3)	90
Volume [Å³]	6370.7(8)	1664.04(14)
Z	6	2
ρ_{calc} [gcm⁻³]	1.291	1.350
μ [mm⁻¹]	0.403	0.490
F(000)	2612	708
Crystal size [mm³]	0.417×0.320×0.145	0.303×0.189×0.166
Crystal colour	orange	orange
Crystal shape	block	block
Radiation	MoK _α (λ=0.71073 Å)	MoK _α (λ=0.71073 Å)
2θ range [°]	3.83 to 66.34 (0.65 Å)	5.30 to 55.11 (0.77 Å)
Index ranges	-18 ≤ h ≤ 18 -31 ≤ k ≤ 31 -42 ≤ l ≤ 42	-14 ≤ h ≤ 14 -13 ≤ k ≤ 13 -18 ≤ l ≤ 18
Reflections collected	666505	45540

Independent reflections	48544, $R_{\text{int}} = 0.0583$, $R_{\text{sigma}} = 0.0235$	7574, $R_{\text{int}} = 0.0376$, $R_{\text{sigma}} = 0.0282$
Completeness to $\theta = 25.242^\circ$	99.8 %	99.7 %
Data / Restraints / Parameters	48544/130/1659	7574/7/462
Goodness-of-fit on F^2	1.056	1.045
Final R indexes [$\geq 2\sigma(I)$]	$R_1 = 0.0432$, $wR_2 = 0.1116$	$R_1 = 0.0350$, $wR_2 = 0.0880$
Final R indexes [all data]	$R_1 = 0.0548$, $wR_2 = 0.1207$	$R_1 = 0.0387$, $wR_2 = 0.0913$
Largest peak/hole [$\text{e}\text{\AA}^{-3}$]	1.26/-1.12	1.18/-0.30
Flack X parameter		0.079(17)

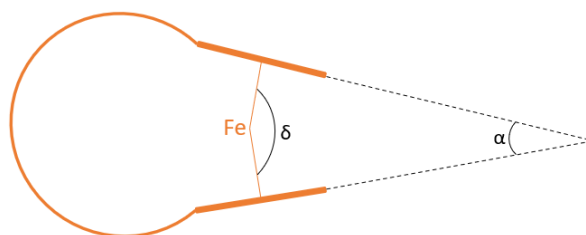


Figure S3.1. Definition of angles α and δ used to characterize structural distortion in ferrocenophanes.

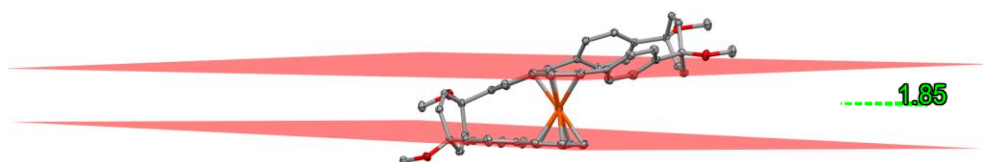


Figure S3.2. Tilt angle α between Cp rings in **pro-Fc[6]CPP** (conformer 2, enantiomer 1) (thermal ellipsoids shown at 50% probability; all hydrogen atoms and solvent were omitted for clarity).

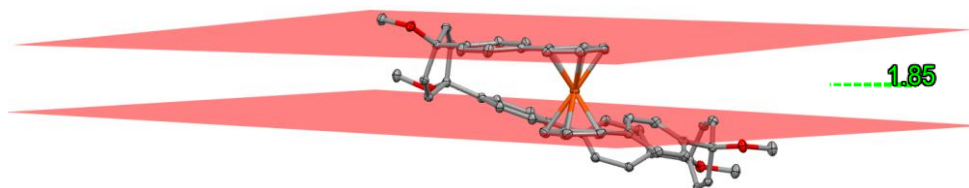
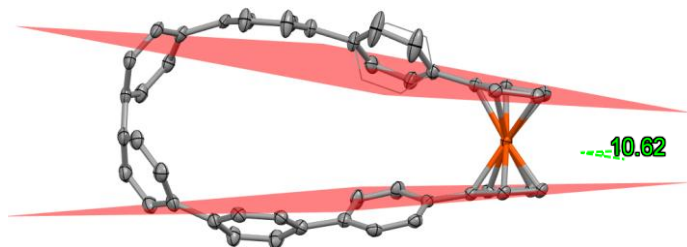
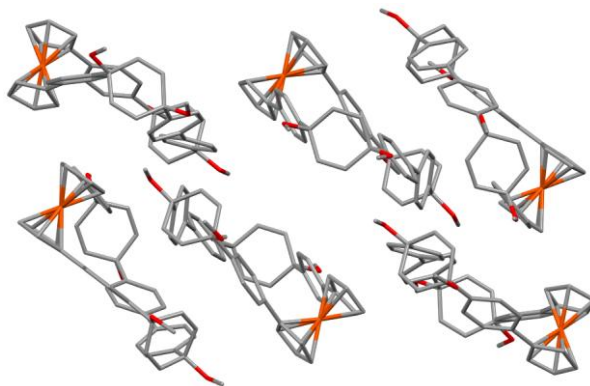


Figure S3.3. Tilt angle α between Cp rings in **pro-Fc[6]CPP** (conformer 2, enantiomer 2) (thermal ellipsoids shown at 50% probability; all hydrogen atoms and solvent were omitted for clarity).

Table S3.2. Angles α and δ in different conformers of **pro-Fc[6]CPP**.

	α (°)	δ (°)
Conformer 1	0.67	179.75
Conformer 2	1.85	179.09
Conformer 3	4.59	176.81

**Figure S3.4.** Tilt angle α between Cp rings in **Fc[6]CPP** (thermal ellipsoids shown at 50% probability; all hydrogen atoms and solvent were omitted for clarity).**Figure S3.5.** Packing of **pro-Fc[6]CPP** (all hydrogen atoms and solvent were omitted for clarity).

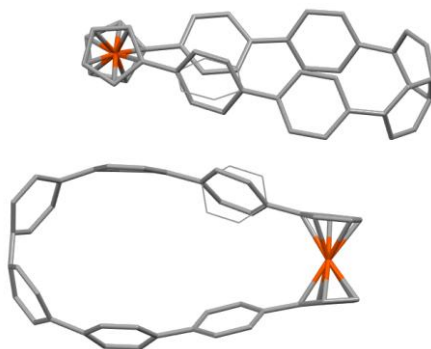


Figure S3.6. Packing of **Fc[6]CPP** (all hydrogen atoms and solvent were omitted for clarity).

3.4.3 Electrochemical measurements

Cyclic voltammetry (CV) and differential pulse voltammetry (DPV) experiments were conducted using a Metrohm Autolab potentiostat running Nova 1.11 software. A glassy carbon working electrode (diameter of electrode disk 2 mm \pm 0.1 mm), a platinum counter electrode and a leakless Ag/AgCl reference electrode were used. Measurements of CH_2Cl_2 solutions of a sample (1 mM) were conducted at room temperature under a N_2 atmosphere in the dark in the presence of a supporting electrolyte ($n\text{-Bu}_4\text{NPF}_6$, 0.1 M). Degassed (3 \times freeze-pump-thaw cycle) CH_2Cl_2 was used. Supporting electrolyte $n\text{-Bu}_4\text{NPF}_6$ was recrystallized from ethanol three times. After the measurement, ferrocene (Fc) was added to the sample solution and the potentials were calibrated with respect to the ferrocene/ferrocenium couple (Fc/Fc^+) vs Ag/AgCl.

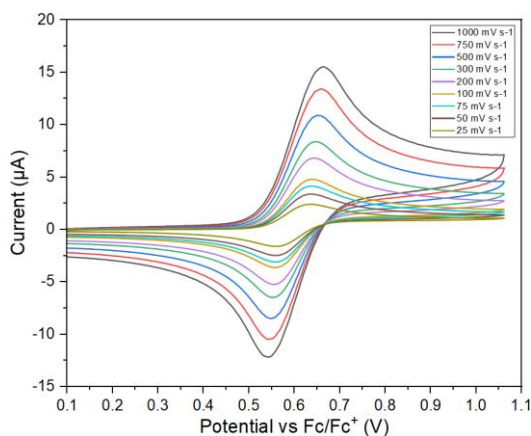


Figure S3.7. Cyclic voltammetry of **Fc[6]CPP** recorded in 0.1 M $n\text{-Bu}_4\text{NPF}_6/\text{CH}_2\text{Cl}_2$ at different scan rates (referenced against Fc/Fc^+).

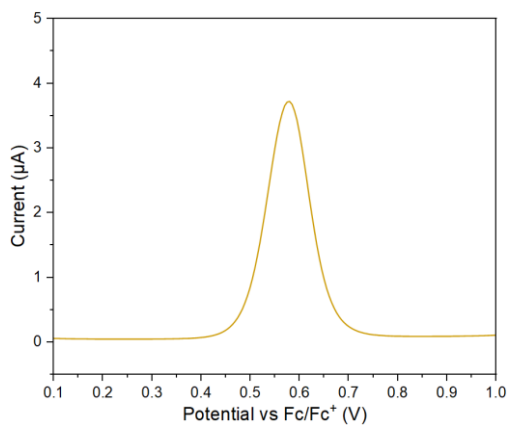


Figure S3.8. Differential pulse voltammetry of **Fc[6]CPP** recorded in 0.1 M *n*-Bu₄NPF₆/CH₂Cl₂ at a scan rate of 100 mV s⁻¹ (referenced against Fc/Fc⁺).

Table S3.3. $E_{1/2}$ values of **Fc[6]CPP** obtained by CV and DPV and referenced against Fc/Fc⁺ (three independent samples).

Measurement	$E_{1/2}$ vs Fc/Fc ⁺ (mV) (from CV at $\nu = 100$ mV s ⁻¹)	$E_{1/2}$ vs Fc/Fc ⁺ (mV) (from DPV at $\nu = 10$ mV s ⁻¹)
1	-49	-60
2	-34	-50
3	-40	-60
Average \pm STD^a	-41.0 \pm 6.2	-56.7 \pm 4.7

^a STD = standard deviation of the mean.

The reversibility was assessed by plotting the square root of the scan rate (ν) against the anodic peak current ($i_{p,a}$) from CV (Randles–Ševčík equation).

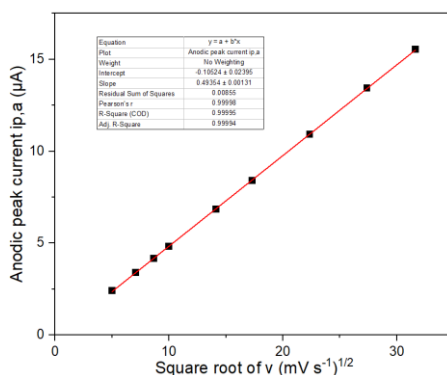


Figure S3.9. Square root of the scan rate (ν) against the anodic peak current ($i_{p,a}$) showing the reversibility of **Fc[6]CPP** oxidation.

3.4.4 Photophysical studies

3.4.4.1 Absorption spectra

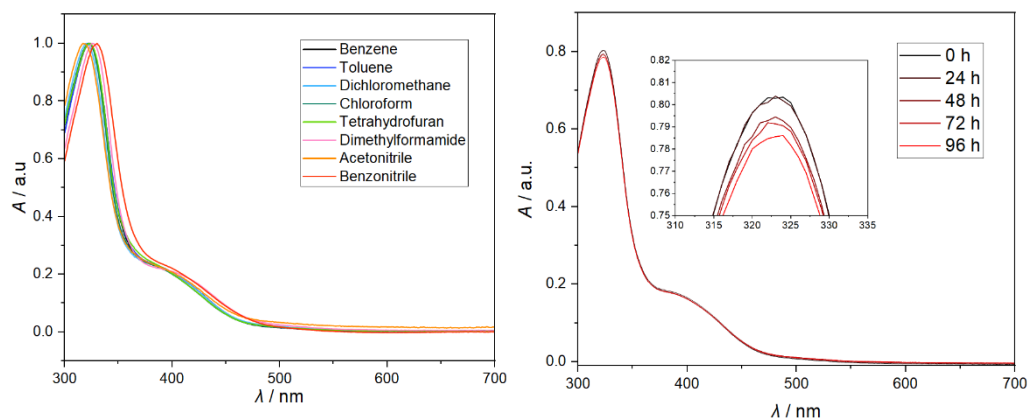


Figure S3.10 (left). Normalized absorption spectra of Fc[6]CPP ($\approx 20 \mu\text{M}$) in different solvents.

Figure S3.11 (right). Absorption spectra of Fc[6]CPP in toluene ($\approx 20 \mu\text{M}$) exposed to daylight over 96 h. Inset shows the zoomed maxima.

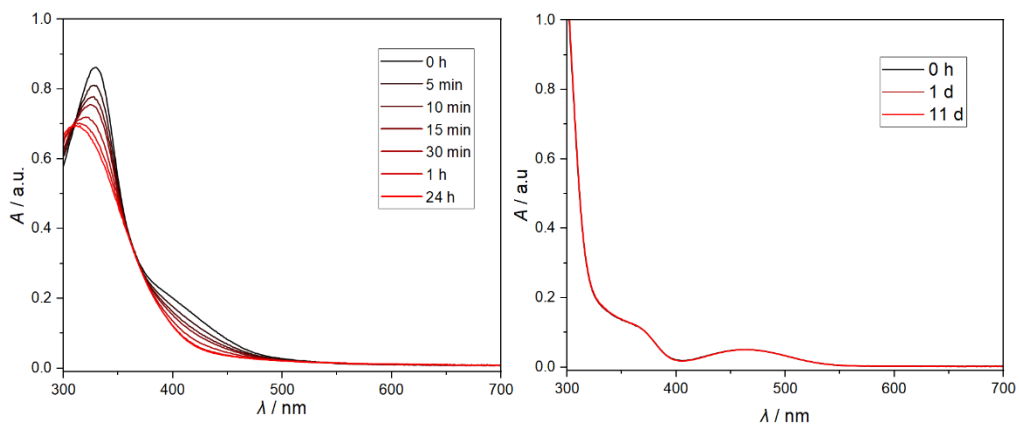


Figure S3.12 (left). Absorption spectra of Fc[6]CPP in PhCN ($\approx 20 \mu\text{M}$) irradiated with 525 nm light.

Figure S3.13 (right). Absorption spectra of pro-Fc[6]CPP in PhCN ($\approx 40 \mu\text{M}$) exposed to daylight over 11 days.

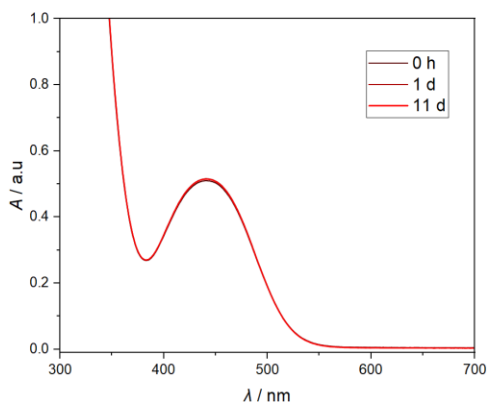


Figure S3.14. Absorption spectra of **Fc** in PhCN (≈ 6.5 mM) exposed to daylight over 11 days.

3.4.4.2 HRMS spectra of photolyzed solution

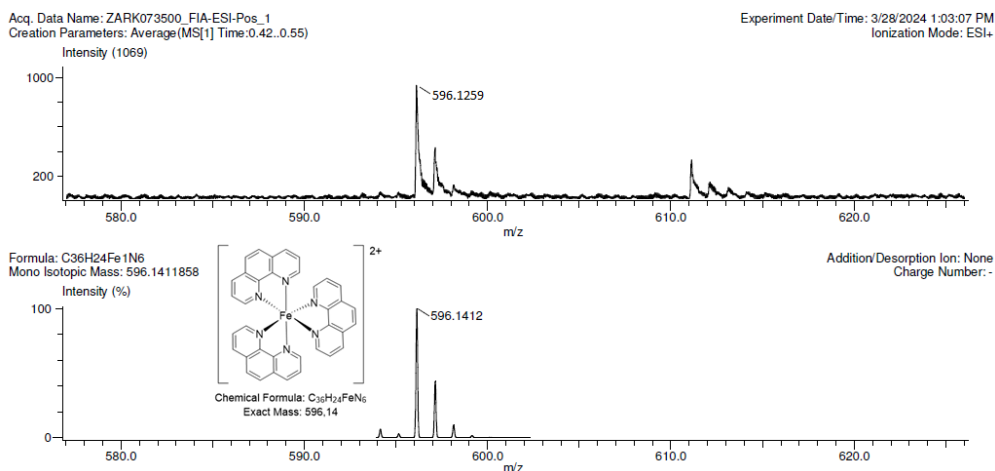


Figure S3.15. HRMS spectrum of $[\text{Fe}(\text{phen})_3]^{2+}$ complex obtained after stirring a **Fc[6]CPP** solution in PhCN (≈ 60 μM) with phen (500 equiv.) in ambient light at room temperature for 24 h (top: obtained spectrum, bottom: simulated spectrum).

3.4.4.3 Chemical yields of $[\text{Fe}(\text{phen})_3]^{2+}$ complex formation

The $[\text{Fe}(\text{phen})_3]^{2+}$ complex solution was prepared by reacting $\text{Fe}(\text{OTf})_2$ (20.00 mg, 0.057 mmol, 1 equiv.) with 1,10-phenanthroline (phen) (50.91 mg, 0.283 mmol, 5 equiv.) in 10.00 mL of PhCN ($c = 0.00565$ M) over 24 h at room temperature. This solution was used to prepare five samples with concentrations between 20–100 μM which were used to measure absorption spectra. The

obtained value ϵ (513 nm) = 11 171 L mol⁻¹ cm⁻¹ is similar to values from literature: ϵ (510 nm) = 11 500 L mol⁻¹ cm⁻¹ in water^[69] and ϵ (510 nm) = 11 100 L mol⁻¹ cm⁻¹ (solvent not indicated).^[70]

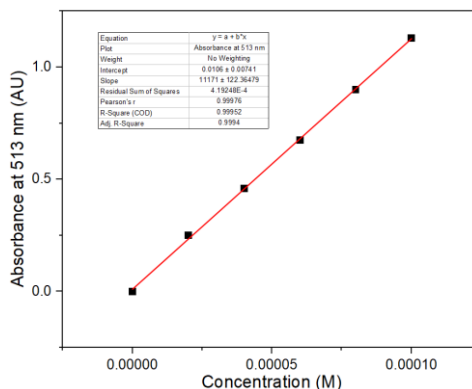


Figure S3.16. Determination of the molar extinction coefficient ϵ of $[\text{Fe}(\text{phen})_3]^{2+}$ complex in PhCN.

General procedure for sample preparation

To a 60 μM sample of **Fc[6]CPP** in PhCN was added 500 equiv. of phen (180 μl , 0.5 M phen solution in PhCN). The sample (total volume = 3.00 mL) was prepared in a quartz cuvette covered in aluminum foil and then stirred in ambient light for 24 h. After this time, the sample was filtered twice through a 0.22 μm PTFE syringe filter. The experiment was repeated four times (Table S3.4). The same procedure was applied to calculate the yield in H₂O/THF with $\epsilon_{450 \text{ nm}} = 4\,049 \text{ mol}^{-1} \text{ cm}^{-1}$ for **Fc[6]CPP** and $\epsilon_{511 \text{ nm}} = 10\,734 \text{ mol}^{-1} \text{ cm}^{-1}$ for $[\text{Fe}(\text{phen})_3]^{2+}$ complex.

Example of calculation of yield of $[\text{Fe}(\text{phen})_3]^{2+}$ complex formation (before and after filtration):

$$\text{yield (before filtration)} = \frac{\text{concentration } ([\text{Fe}(\text{phen})_3]^{2+}) \text{ at } t = 24 \text{ h}}{\text{concentration } (\text{Fc}[6]\text{CPP}) \text{ at } t = 0 \text{ h}} =$$

$$\frac{\frac{A_{[\text{Fe}(\text{phen})_3]^{2+}}}{\epsilon_{513 \text{ nm}}}}{\frac{A_{\text{Fc}[6]\text{CPP}}}{\epsilon_{450 \text{ nm}}}} = \frac{\frac{0.5334}{11171}}{\frac{0.2731}{4708}} = 82.31\%$$

$$\text{yield (after filtration)} = \frac{\text{concentration } ([\text{Fe}(\text{phen})_3]^{2+}) \text{ at } t = 24 \text{ h}}{\text{concentration } (\text{Fc}[6]\text{CPP}) \text{ at } t = 0 \text{ h}} =$$

$$\frac{\frac{A_{[Fe(phen)_3]^{2+}}}{\epsilon_{513 \text{ nm}}}}{\frac{A_{Fc[6]CPP}}{\epsilon_{450 \text{ nm}}}} = \frac{0.4211}{\frac{11171}{4708}} = 64.99\%$$

Table S3.4. Chemical yield of $[Fe(phen)_3]^{2+}$ complex formation before and after filtration.

Experiment	Yield before filtration (%)	Yield after filtration (%)
1	82.31	64.99
2	75.91	60.40
3	83.77	66.64
4	79.32	74.70
Average \pm STD^a	80.3 \pm 3.01	66.7 \pm 5.16

^aSTD = standard deviation of the mean.

3.4.4.4 Control experiments w/o light

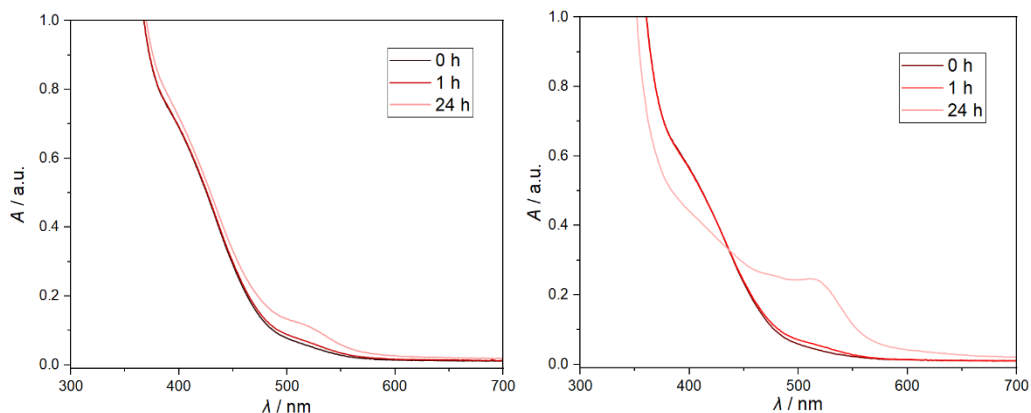


Figure S3.17 (left). Fc[6]CPP in PhCN ($\approx 60 \mu\text{M}$) with phen (500 equiv.) stirred in dark at room temperature.

Figure S3.18 (right). Fc[6]CPP in PhCN ($\approx 60 \mu\text{M}$) with phen (500 equiv.) stirred in dark at 70°C .

3.4.4.5 Quantum yields of $[Fe(phen)_3]^{2+}$ complex formation

A solution of Fc, pro-Fc[6]CPP or Fc[6]CPP (see sample preparation below) in PhCN was stirred and left to equilibrate for 2–3 min in the dark at 20°C . Afterward, the sample was irradiated with

a beam of collimated light at 472 nm ($\varnothing=7$ mm) using a FC1-LED 470CG light source (Figure S3.19) coupled to a polymer optical fibre from Prizmatix.^[71] UV-vis spectra were recorded periodically using diode-array spectrophotometer. The radiant power (flux; Φ_e) of the light source was determined using calibrated Si-photodiode and optical power meter. The total irradiation time was selected to reach <10% conversion and to obtain 6–10 experimental points. The procedure was repeated 2–4 times. The quantum yield of formation Φ_{form} was calculated according to the equation:

$$\Phi_{form} = \frac{\Delta n_{form}}{\Delta n_{abs}^p} \quad (\text{Eq. 1})$$

where Δn_{form} is the number of moles of $[\text{Fe}(\text{phen})_3]^{2+}$ complex formed, calculated from the absorbance change at λ_{max} (513 nm), and Δn_{abs}^p is the number of moles of photons absorbed by the sample in the given time period calculated according to the equation:

$$\Delta n_{abs}^p = \frac{\int_0^t \int_0^\infty (1 - 10^{-A(\lambda,t)}) I_\lambda^{em} d\lambda dt}{6.022 \times 10^{23}} \quad (\text{Eq. 2})$$

where $A(\lambda,t)$ is the absorbance of the sample at the wavelength λ in time t , and I_λ^{em} is the photon flux of the LED source at the wavelength λ determined according to the equation:

$$I_\lambda^{em} = q_n(\lambda) \frac{\Phi_e}{\int_0^\infty \frac{hc}{\lambda} q_n(\lambda) d\lambda} \quad (\text{Eq. 3})$$

where $q_n(\lambda)$ is the emission spectrum of the LED source provided by manufacturer (counts vs. wavelength) and Φ_e is the radiant power (flux) measured by the optical power meter.

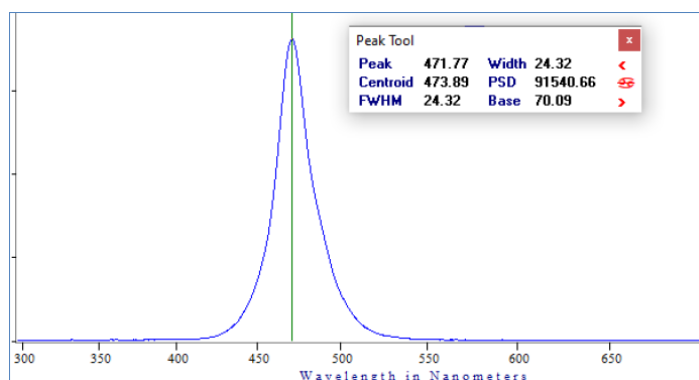


Figure S3.19. Emission spectrum of the FC1-LED 470CG light source (obtained from Prizmatix^[71]).

General procedure for sample preparation

Fc: to a 40 μM solution of **Fc** in PhCN was added 500 equiv. of phen (120 μL , 0.5 M phen solution in PhCN). The sample (total volume = 3.00 mL) was prepared in a quartz cuvette covered in aluminum foil and then irradiated (472 nm, $\phi_e = 130.2$ mW) for ~ 1.5 h while stirring. The experiment was repeated four times.

pro-Fc[6]CPP: to a 40 μM solution of **pro-Fc[6]CPP** in PhCN was added 500 equiv. of phen (120 μL , 0.5 M phen solution in PhCN). The sample (total volume = 3.00 mL) was prepared in a quartz cuvette covered in aluminum foil and then irradiated (472 nm, $\phi_e = 130.2$ mW) for 0.5 h while stirring. The experiment was repeated four times.

Fc[6]CPP: to a 40 μM solution of **Fc[6]CPP** in PhCN was added phen:

was prepared in a quartz cuvette by adding 76 μL (1 equiv.) of 1.56 mM **Fc[6]CPP** solution in PhCN to phen solution in PhCN and PhCN (total volume = 3.00 mL):

- 5 equiv. (20 μL , 0.0296 M solution in PhCN)
- 10 equiv. (40 μL , 0.0296 M solution in PhCN) (effect of oxygen)
- 25 equiv. (100 μL , 0.0296 M solution in PhCN)
- 100 equiv. (24 μL , 0.5 M solution in PhCN)
- 250 equiv. (60 μL , 0.5 M solution in PhCN)
- 500 equiv. (120 μL , 0.5 M solution in PhCN)

The sample (total volume = 3.00 mL) was prepared in a quartz cuvette covered in aluminum foil and then irradiated (472 nm, $\phi_e = 9.86 - 46.4$ mW) for 1 or 2 min while stirring. The experiment was repeated two or four times. The same procedure was applied to calculate the quantum yield in $\text{H}_2\text{O}/\text{THF}$.

Table S3.5. Quantum yields of $[\text{Fe}(\text{phen})_3]^{2+}$ complex formation from **Fc**, **pro-Fc[6]CPP** and **Fc[6]CPP** in PhCN in the presence of phen upon irradiation with a 472 nm light source.

Compd.	phen (equiv.)	Φ_e (mW)	Φ_{form}	Average	STD ^a
Fc	500	130.2	$1.70 \cdot 10^{-5}$	$1.52 \cdot 10^{-5}$	$2.62 \cdot 10^{-6}$
			$1.11 \cdot 10^{-5}$		
			$1.79 \cdot 10^{-5}$		
			$1.48 \cdot 10^{-5}$		
Fc	500	130.2	$1.45 \cdot 10^{-5 b}$	$2.02 \cdot 10^{-5 b}$	n.d. ^c
			$2.42 \cdot 10^{-5 b}$		
			$2.50 \cdot 10^{-5 b}$		
			$1.71 \cdot 10^{-5 b}$		
pro-Fc[6]CPP	500	130.2	$5.39 \cdot 10^{-5}$	$4.91 \cdot 10^{-5}$	$3.99 \cdot 10^{-6}$
			$5.20 \cdot 10^{-5}$		
			$4.40 \cdot 10^{-5}$		
			$4.66 \cdot 10^{-5}$		
Fc[6]CPP	5	46.4	0.0017	$1.57 \cdot 10^{-3}$	$1.19 \cdot 10^{-4}$
			0.00138		
			0.00155		
			0.00163		
	25	25.6	0.00781	$6.96 \cdot 10^{-3}$	$8.55 \cdot 10^{-4}$
			0.0061		
	100	9.86	0.0357	$3.41 \cdot 10^{-2}$	$3.12 \cdot 10^{-3}$
			0.0371		
0.0347					
0.0289					
250	9.86	0.0483	$5.27 \cdot 10^{-2}$	$4.35 \cdot 10^{-3}$	
		0.057			
500	9.86	0.0601	$6.00 \cdot 10^{-2}$	$4.88 \cdot 10^{-3}$	
		0.0669			
		0.0531			
		0.0597			

^a STD = standard deviation of the mean. ^b Calculated manually using the same datasets measured for the samples of **Fc**, but assuming the lightsource was monochromatic (472 nm) and the absorbed photons were obtained from Lambert-Beer law to verify the validity of the used script, which employed equations 1–3. ^c n.d. = not determined.

Representative examples of the obtained slopes (= quantum yields):

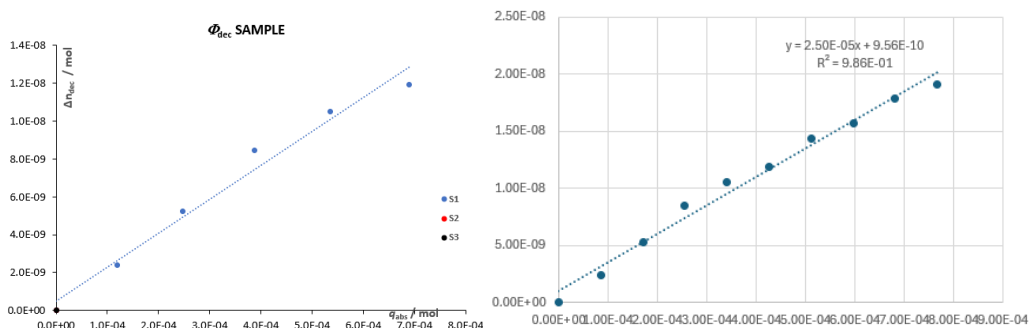


Figure S3.20 (left). Fc + phen (500 equiv.).

Figure S3.21 (right). Fc + phen (500 equiv.) assuming the lightsource was monochromatic (472 nm) and the absorbed photons calculated from Lambert-Beer law to verify the validity of the used computer script based on equations 1–3.

$$\Phi_{\text{form}} = 5.39E-05 \pm 0.0E+00$$

$$\Phi_{\text{form}} = 1.55E-03 \pm 0.0E+00$$

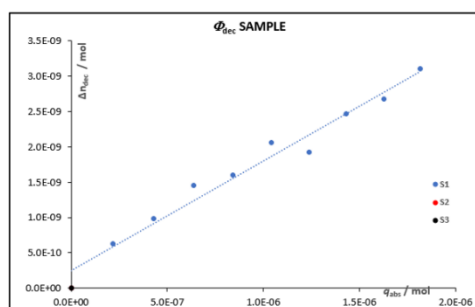
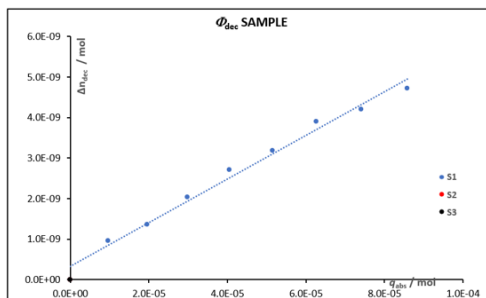
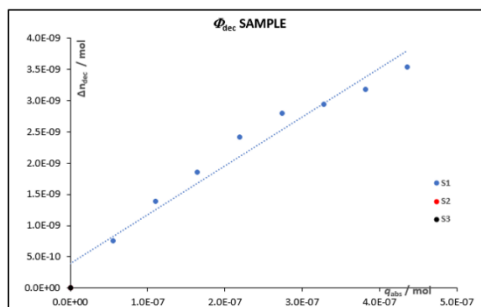


Figure S3.22 (left). Pro-Fc[6]CPP + phen (500 equiv.). Note that the error is not reported because a single dataset is displayed.

Figure S3.23 (right). Fc[6]CPP + phen (5 equiv.). Note that the error is not reported because a single dataset is displayed.

$$\Phi_{\text{form}} = 7.81\text{E-}03 \pm 0.0\text{E+}00$$



$$\Phi_{\text{form}} = 3.57\text{E-}02 \pm 0.0\text{E+}00$$

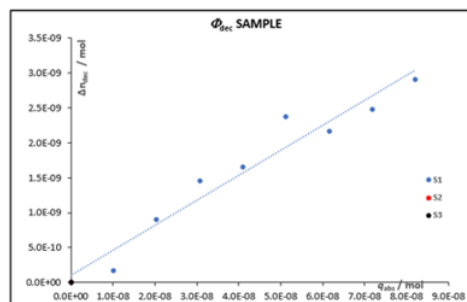
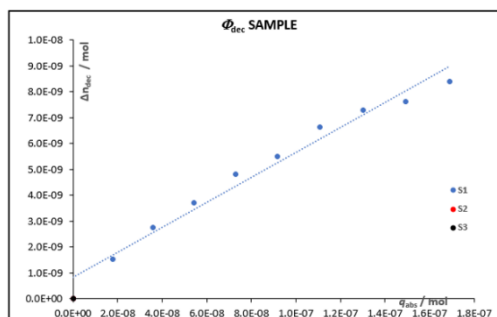


Figure S3.24. Fc[6]CPP + phen (25 equiv.). Note that the error is not reported because a single dataset is displayed.

Figure S3.25. Fc[6]CPP + phen (100 equiv.). Note that the error is not reported because a single dataset is displayed.

$$\Phi_{\text{form}} = 4.83\text{E-}02 \pm 0.0\text{E+}00$$



$$\Phi_{\text{form}} = 6.01\text{E-}02 \pm 0.0\text{E+}00$$

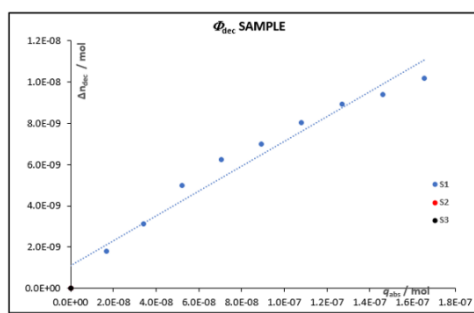


Figure S3.26 (left). Fc[6]CPP + phen (250 equiv.). Note that the error is not reported because a single dataset is displayed.

Figure S3.27 (right). Fc[6]CPP + phen (500 equiv.). Note that the error is not reported because a single dataset is displayed.

3.4.4.6 Quantum yield simulations

Assuming that $[\text{Fe}(\text{phen})_3]^{2+}$ formation from **Fc[6]CPP** occurs via its triplet state, the quantum yield of $[\text{Fe}(\text{phen})_3]^{2+}$ complex formation Φ_{form} can be written as:

$$\Phi_{form} = \Phi_{ISC} \cdot \Phi_{phen}$$

where Φ_{ISC} ($= 0.085$)^[53] is the quantum yield of intersystem crossing reported for **Fc** ($E_T \sim 40$ kcal mol⁻¹) and Φ_{phen} is the quantum yield of quenching of the excited T₁ state by phen which can be defined (in the presence of oxygen) as:

$$\Phi_{phen} = \frac{k_{diff} \cdot [\text{phen}]}{\frac{1}{\tau_{T_1}} + k_{diff} \cdot [\text{phen}] + k_{diff} \cdot [O_2]}$$

where k_{diff} ($\approx 5 \times 10^{10}$ M⁻¹ s⁻¹) is the approximate diffusion rate constant in PhCN, τ_{T_1} ($= 9 \times 10^{-8}$ s)^[53] is the lifetime of the T₁ state reported for **Fc**. Thus, Φ_{form} can be defined as:

$$\Phi_{form} = \Phi_{ISC} \cdot \frac{k_{diff} \cdot [\text{phen}]}{\frac{1}{\tau_{T_1}} + k_{diff} \cdot [\text{phen}] + k_{diff} \cdot [O_2]}$$

This equation was used to calculate Φ_{form} from **Fc[6]CPP** in the presence ($[O_2] \approx 2.5 \times 10^{-3}$ M) and the absence of oxygen ($[O_2] = 0$ M) for concentrations of phenanthroline ranging from 2×10^{-4} M to 2×10^{-2} M (corresponding to 5 to 500 equiv. in the experiments performed in section 5.6).

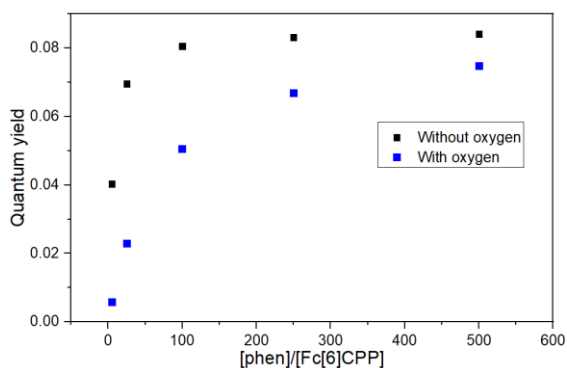


Figure S3.28. Simulations of quantum yields of $[\text{Fe}(\text{phen})_3]^{2+}$ formation from **Fc[6]CPP** and different equivalents of phen in the absence and the presence of oxygen.

The quantum yields of $[\text{Fe}(\text{phen})_3]^{2+}$ complex formation from **Fc[6]CPP** with 10 or 25 equiv. of phen in PhCN in the presence and the absence of oxygen were determined using the procedure described in section 5.6. Prior to the measurement, the sample was either oxygenated by bubbling

with oxygen or degassed by bubbling with nitrogen for 20 min. The sample was then irradiated (472 nm) for 20 sec while stirring. Each experiment was repeated at least four times.

3.4.4.7 Mechanistic insights

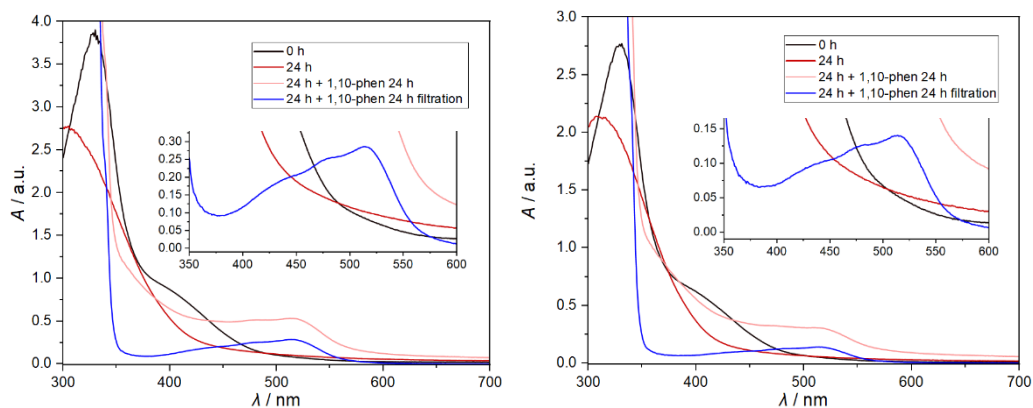


Figure S3.29 (right). Fc[6]CPP in PhCN ($\approx 60 \mu\text{M}$) stirred in ambient light for 24 h, followed by addition of phen (500 equiv.) and stirring in ambient light.

Figure S3.30 (left). Fc[6]CPP in PhCN ($\approx 60 \mu\text{M}$) stirred in ambient light for 24 h, followed by addition of phen (500 equiv.) and stirring in dark.

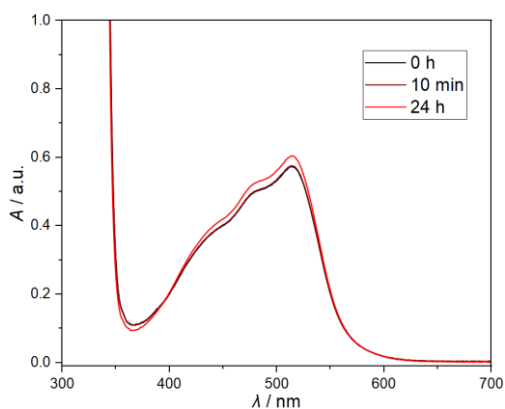


Figure S3.31. Fe(OTf)₂ + phen (500 equiv.) in PhCN ($\approx 60 \mu\text{M}$) stirred in ambient light for 24 h.

3.4.4.8 Experiments in THF/H₂O

The experiments requiring irradiation with green light ($\lambda_{\text{LED}} = 525 \text{ nm}$, FWHM = 35 nm) were done using the PR160L-525 LED lamp (25 % intensity) purchased from Kessil.^[72] The samples were placed 20 cm away from the light source.

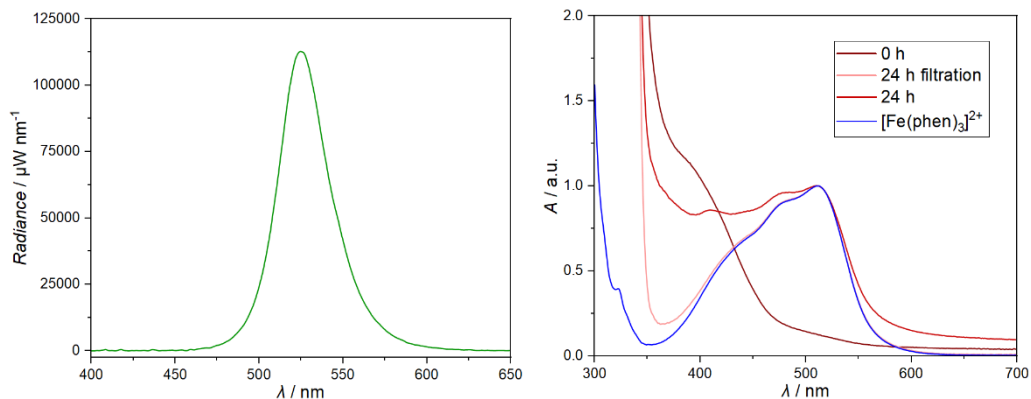


Figure S3.32 (left). Emission spectrum of the PR160L-525 LED lamp (obtained from Kessil^[72]).

Figure S3.33 (right). Normalized absorption spectra of **Fc[6]CPP** in H₂O/THF ($v/v = 1:1$, $\approx 60 \mu\text{M}$, phen: 500 equiv.) stirred in green light ($\lambda_{\text{LED}} = 525 \text{ nm}$) for 24 h (red: unfiltered, light red: filtered) and independently prepared $[\text{Fe}(\text{phen})_3]^{2+}$ (blue). The spectrum of the solution at 0 h (dark red) was scaled such that the absorbance at 400 nm matched the absorbance of $[\text{Fe}(\text{phen})_3]^{2+}$ with equal concentration at its $\epsilon_{\text{max}} = 511 \text{ nm}$.

3.4.5 DFT calculations

3.4.5.1 General remarks

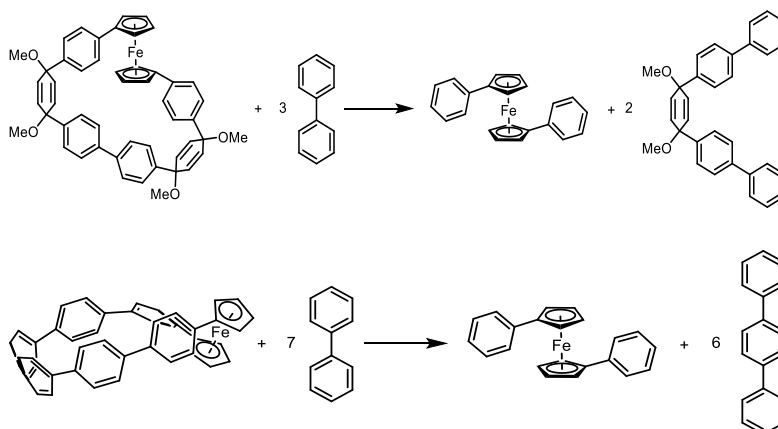
All calculations were performed with Gaussian 16^[73] (release C.02) software. The crystal structures of **pro-Fc[6]CPP** and **Fc[6]CPP** were used as a starting point and geometries were optimized at D3-B3LYP/6-31+g(d)/LanL2DZ(Fe) level of theory. Effective core potential was used for iron atoms. For triplet states, we needed to check and eventually reoptimize the triplet wavefunction. The stable wavefunction was then used to optimize the geometries. The minima on potential energy surface were confirmed by subsequent frequency calculations.

Table S3.6. Geometrical parameters of the studied species as compared to crystal structures.

Compd.	Method	Multiplicity	α (°)	δ (°)	d (Å) ^a
pro-Fc[6]CPP	X-ray	-	0.67	179.75	10.961
	D3-B3LYP	1	0.91	179.73	11.097
		3	1.01	179.46	11.128
Fc[6]CPP	X-ray	-	10.62	172.84	7.004
	D3-B3LYP	1	6.97	175.61	6.920
		3	12.05	173.43	7.236

^a Diameter of the cavity was determined as the distance between centroids of the cyclohexadiene moieties for **pro-Fc[6]CPP** and corresponding phenylenes for **Fc[6]CPP**.

3.4.5.2 Strain energy



Scheme S3.1. Homodesmotic reactions used to calculate strain energy of the **pro-Fc[6]CPP** (top) and **Fc[6]CPP** (bottom).

Table S3.7. Strain energies in kcal mol⁻¹ calculated using 6-31++g(d)/LanL2DZ(Fe) basis sets and the corresponding functional.

Compd.	D3-B3LYP	wB97XD
pro-Fc[6]CPP	13.7	11.4
Fc[6]CPP	82.6	85.5

3.4.5.3 Frontier molecular orbitals

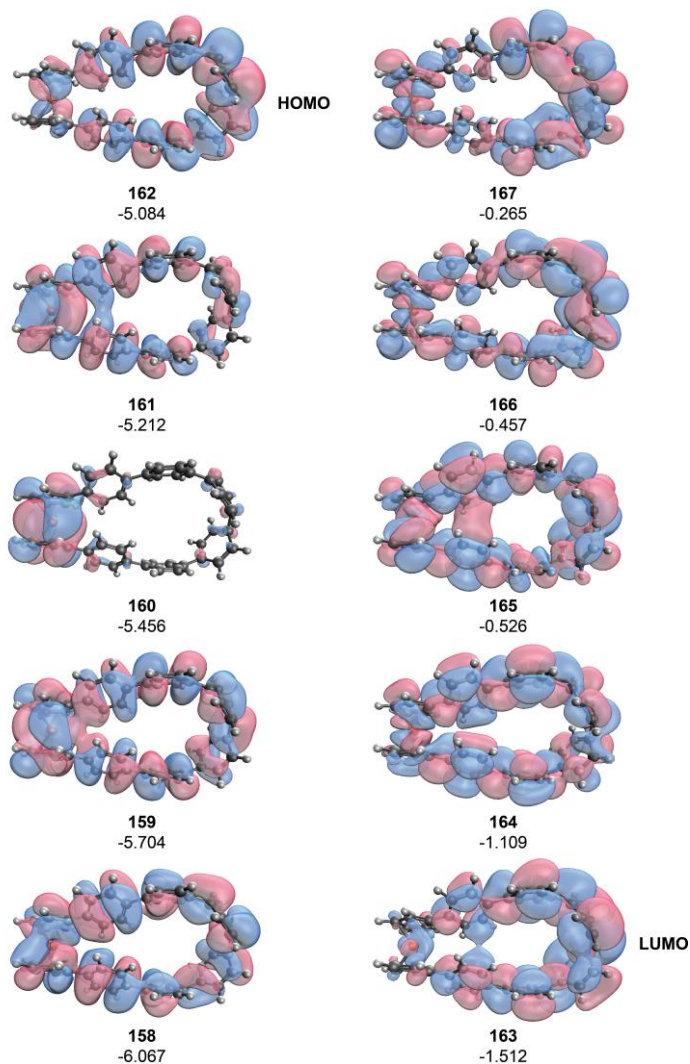


Figure S3.34. Frontier molecular orbitals of **Fc[6]CPP** (singlet) with orbital number and their energy in eV at D3-B3LYP/6-31g(d)/LanL2DZ(Fe) level of theory. Note that the energies of the virtual MOs are only approximate.

3.4.5.4 Spin density plot

Spin density of triplet **Fc[6]CPP** was calculated at (U)-D3-B3LYP/6-31g(d)/LanL2DZ(Fe) level of theory.

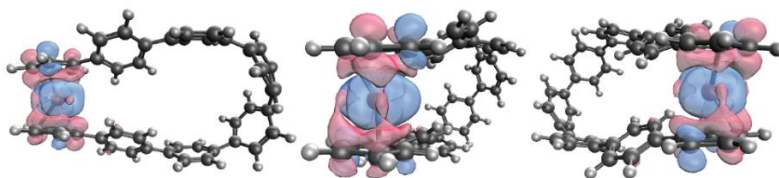


Figure S3.35. Spin density distribution in triplet **Fc[6]CPP** (isosurface value = 0.02).

3.4.5.5 Time dependent DFT calculations

Natural transition orbitals (NTOs) were plotted at the TD-CAM-B3LYP/6-31g(d)/LanL2DZ(Fe) level of theory (isosurface value = 0.02).

Table S3.8. The first 10 transitions of **Fc[6]CPP** at TD-CAM-B3LYP/6-31g(d)/LanL2DZ(Fe) level of theory.

Transition	E (eV)	λ (nm)	μ_f	Orbital contributions ^a
1	1.93	643	0.0007	159->177 (14%)
2	1.94	640	0.0008	159->172 (24%) 160->177 (15%)
3	2.46	503	0.0017	149->177 (12%) 160->172 (26%)
4	2.49	499	0	149->172 (23%) 159->172 (20%)
5	3.40	365	0.0001	149->177 (15%) 160->172 (16%)
6	3.46	358	0.0007	149->172 (43%)
7	3.51	353	0.1661	162->163 (85%) 161->163 (19%)
8	4.29	289	1.2343	162->164 (38%) 162->166 (18%) 155->163 (11%)
9	4.46	278	0.5605	161->163 (23%) 162->166 (21%) 162->169 (10%)
10	4.52	274	0.411	161->164 (47%) 162->165 (13%)

^a Only the contributions larger than 10% or the highest contributing transitions are listed.

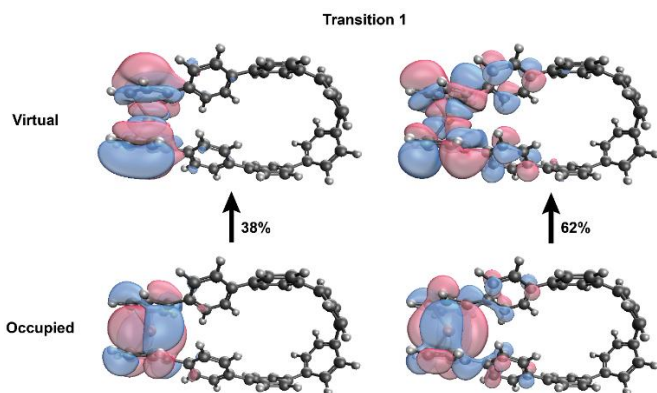


Figure S3.36. NTO of the $S_0 \rightarrow S_1$ transition ($E = 1.93$ eV, $f = 0.0007$) of **Fc[6]CPP**.

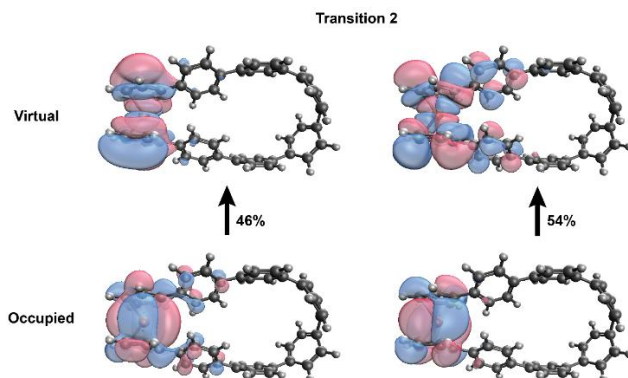


Figure S3.37. NTO of the $S_0 \rightarrow S_2$ transition ($E = 1.94$ eV, $f = 0.0008$) of **Fc[6]CPP**.

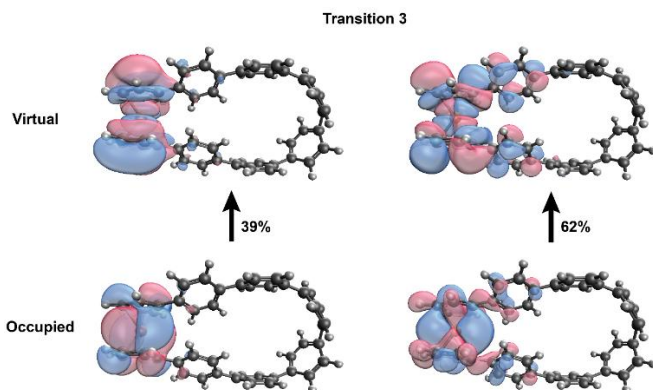


Figure S3.38. NTO of the $S_0 \rightarrow S_3$ transition ($E = 2.46$ eV, $f = 0.0017$) of **Fc[6]CPP**.

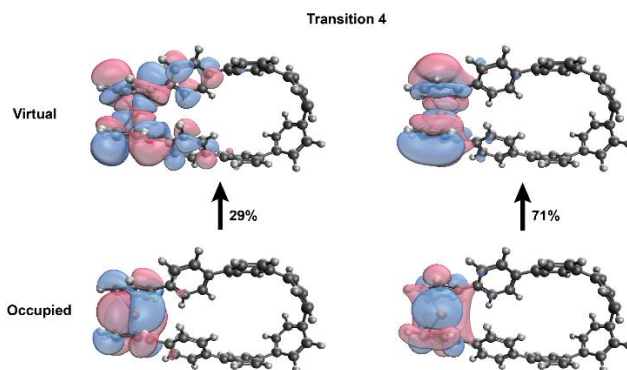


Figure S3.39. NTO of the $S_0 \rightarrow S_4$ transition ($E = 2.49$ eV, $f = 0$) of **Fc[6]CPP**.

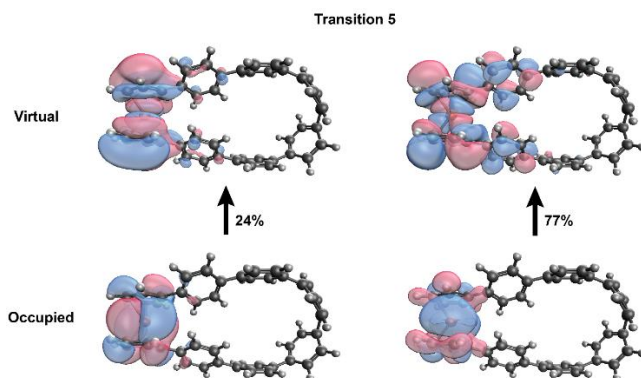


Figure S3.40. NTO of the $S_0 \rightarrow S_5$ transition ($E = 3.40$ eV, $f = 0.0001$) of **Fc[6]CPP**.

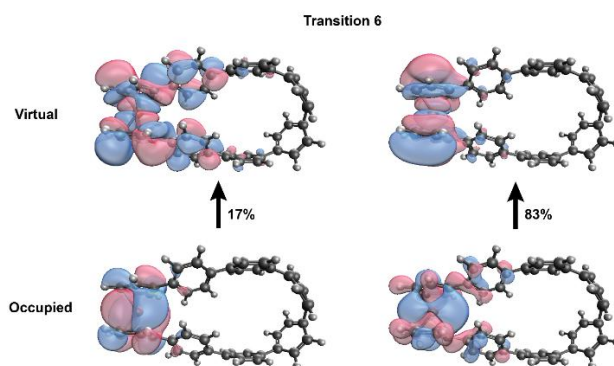


Figure S3.41. NTO of the $S_0 \rightarrow S_6$ transition ($E = 3.46$ eV, $f = 0.0007$) of **Fc[6]CPP** with their occupancies.

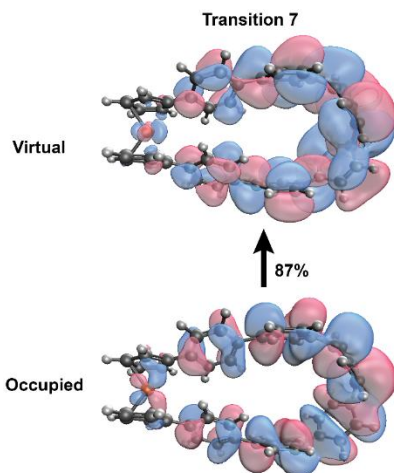
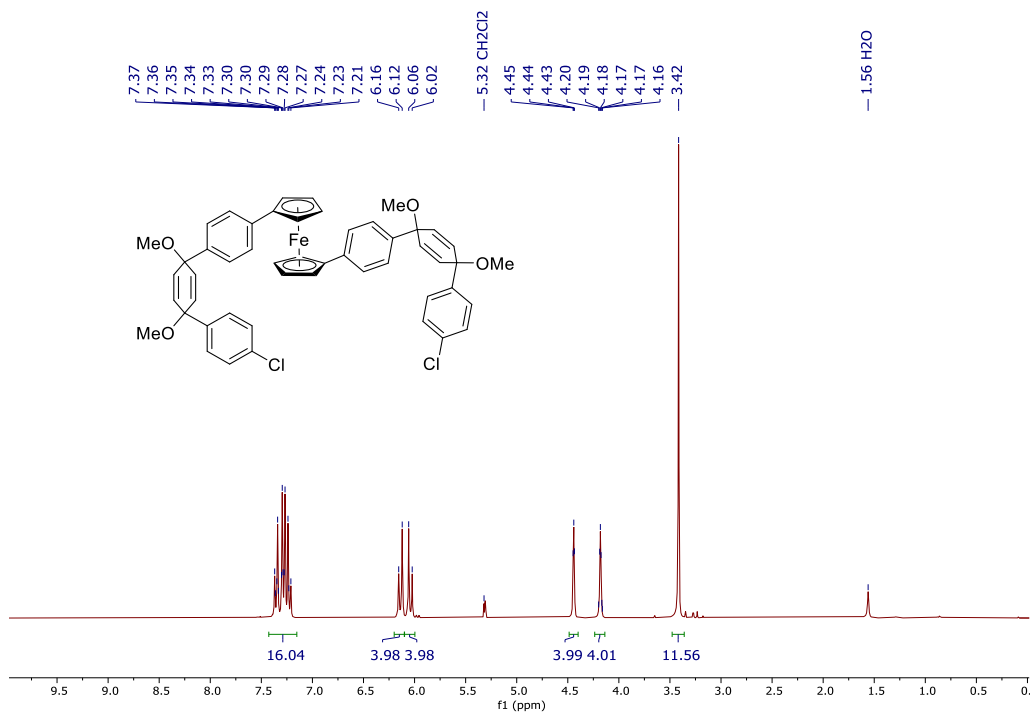
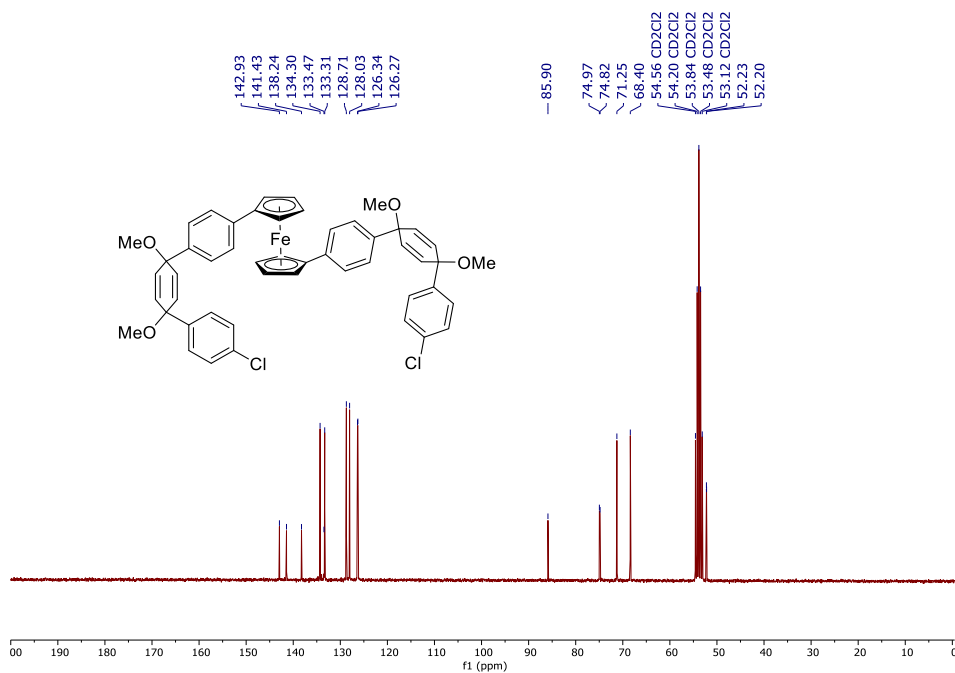


Figure S3.42. NTO of the $S_0 \rightarrow S_7$ transition ($E = 3.51$ eV, $f = 0.1661$) of **Fc[6]CPP** with their occupancies.

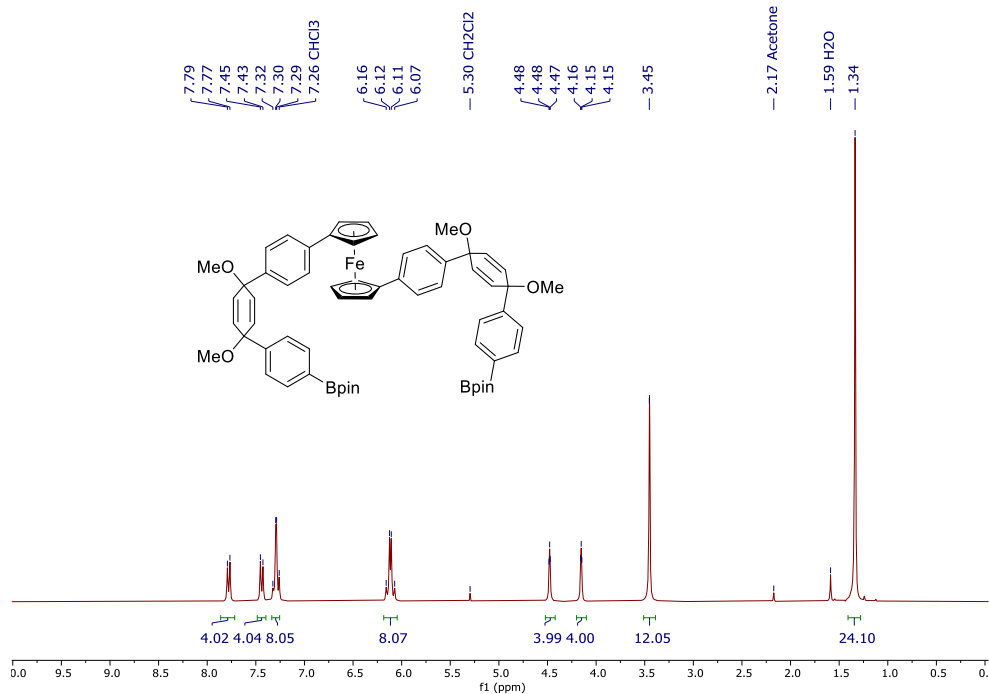
3.4.6 ^1H and ^{13}C NMR spectra



^1H NMR spectrum of compound **2** in CD_2Cl_2 (300 MHz).

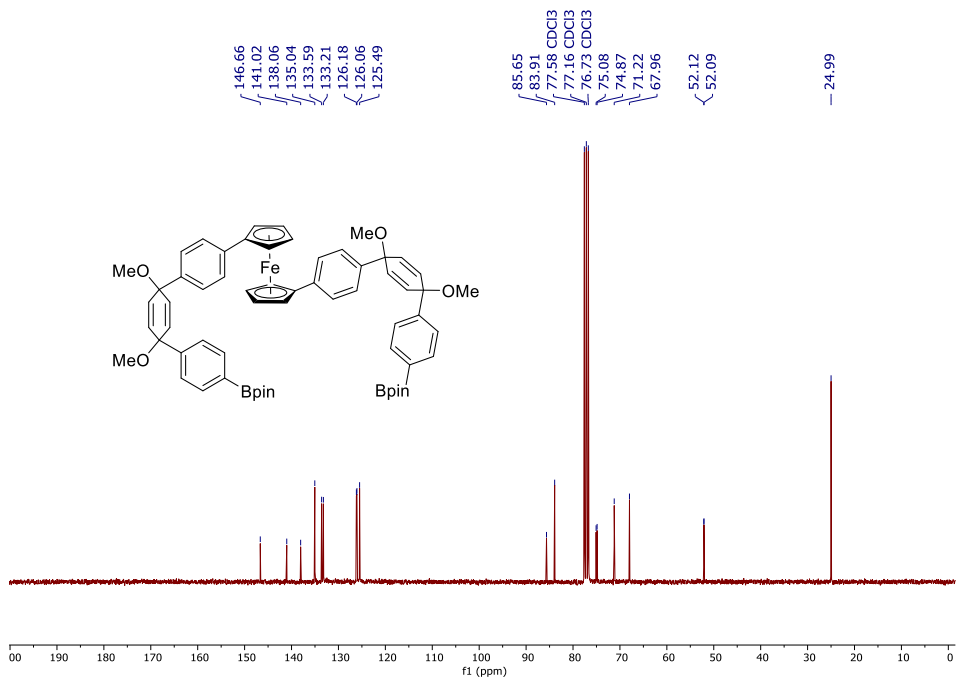


¹³C NMR spectrum of compound **2** in CD₂Cl₂ (75 MHz).

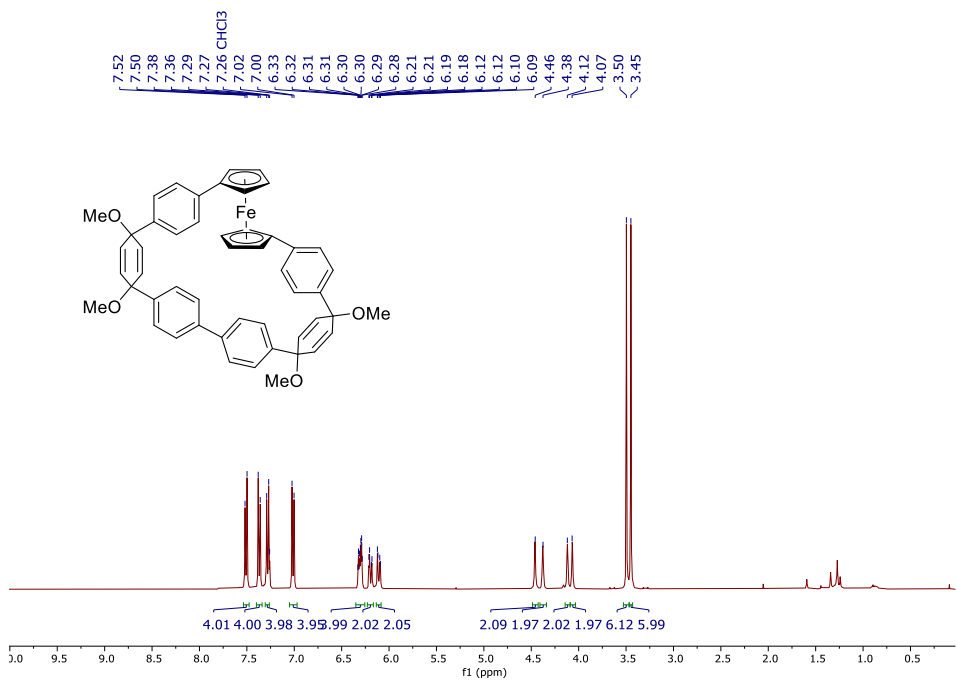


¹H NMR spectrum of compound **3** in CDCl₃ (300 MHz).

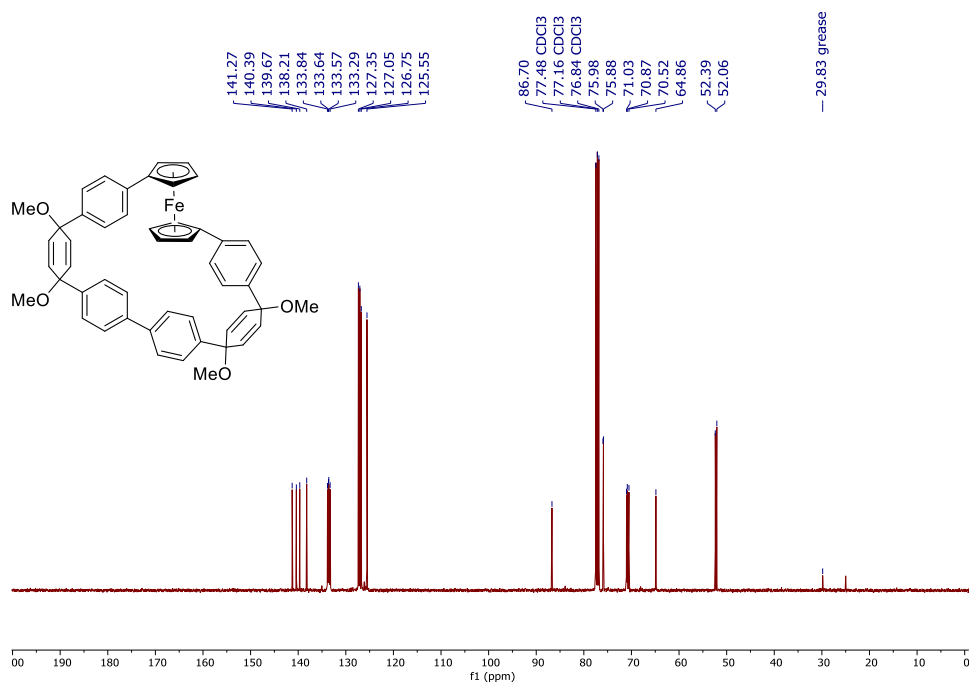
Chapter 3



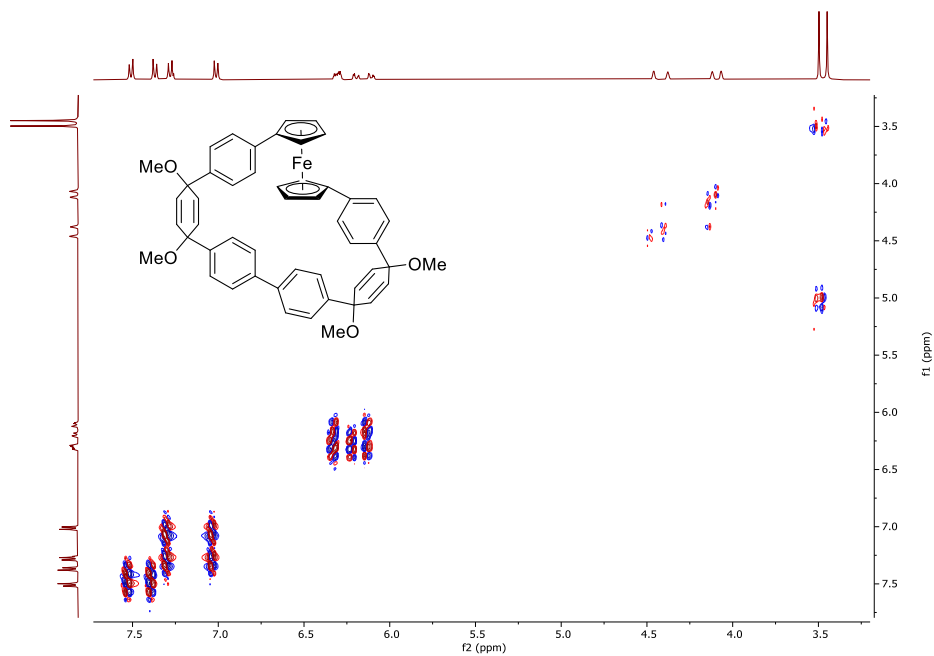
¹³C NMR spectrum of compound **3** in CDCl₃ (101 MHz).



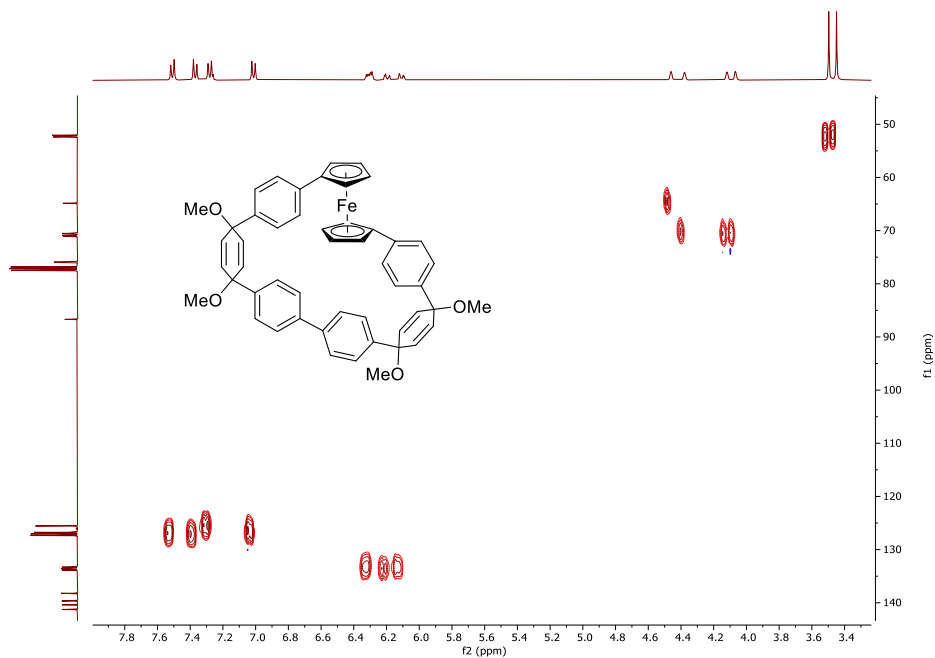
¹H NMR spectrum of **pro-Fc[6]CPP** in CDCl₃ (300 MHz).



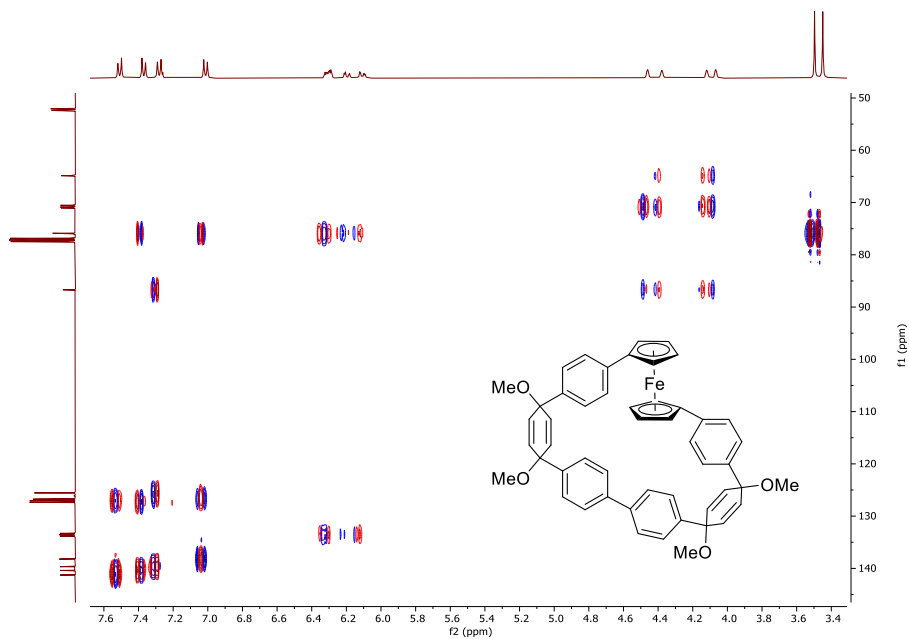
^{13}C NMR spectrum of **pro-Fc[6]CPP** in CDCl_3 (101 MHz).



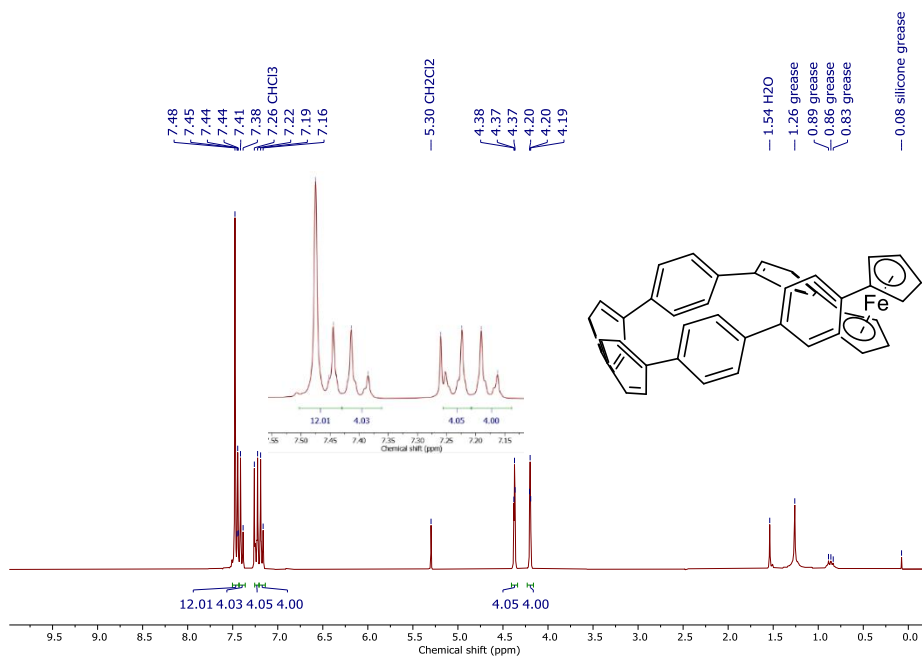
^1H - ^1H COSY spectrum of **pro-Fc[6]CPP** in CDCl_3 (300 MHz).



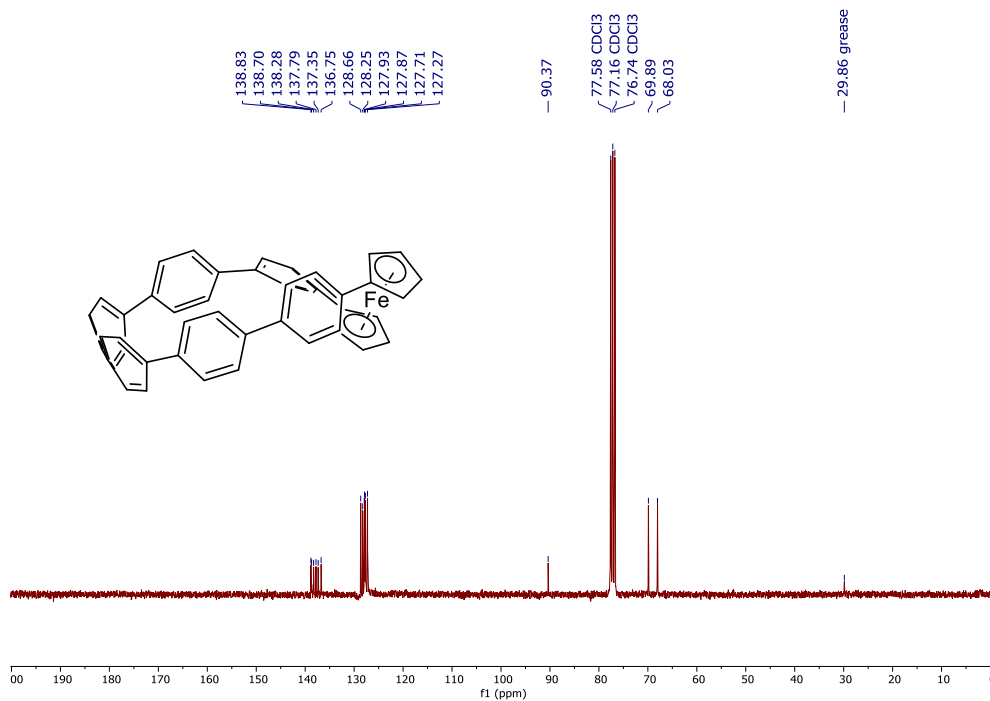
^1H - ^{13}C HSQC spectrum of **pro-Fc[6]CPP** in CDCl_3 (300/101 MHz).



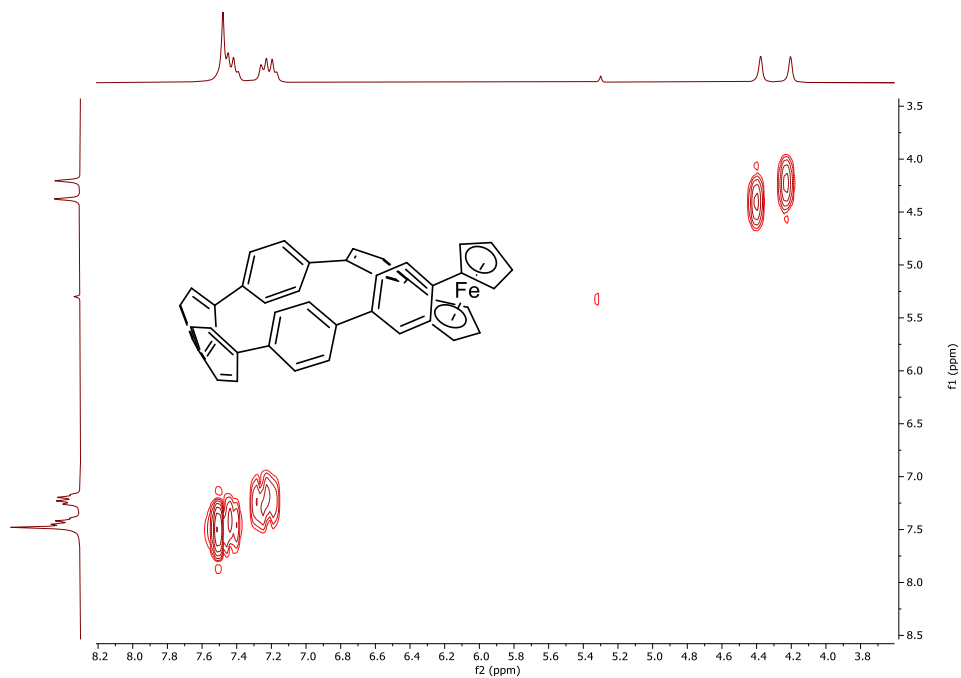
^1H - ^{13}C HMBC spectrum of **pro-Fc[6]CPP** in CDCl_3 (300/101 MHz).



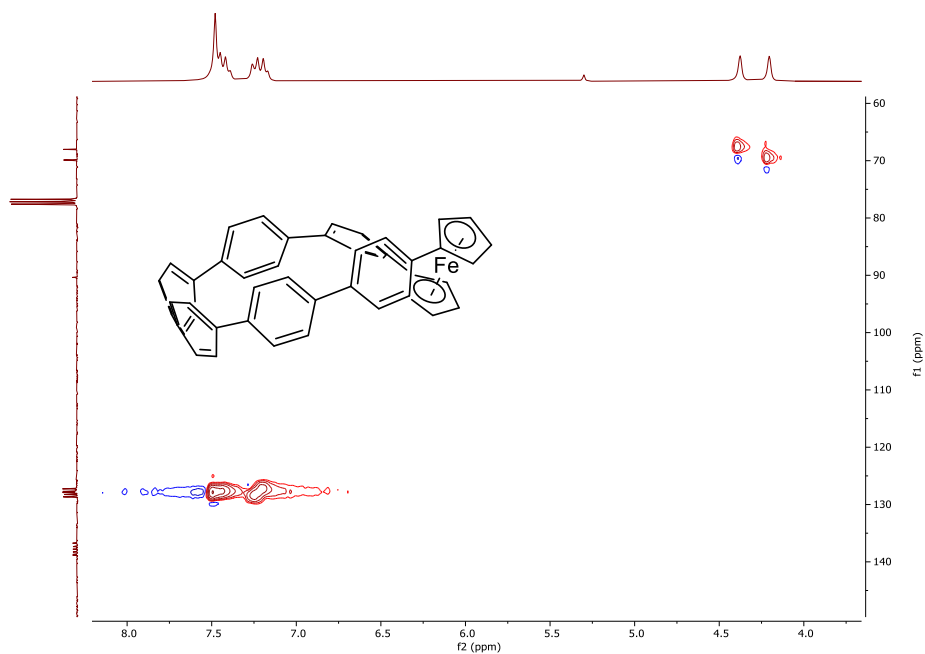
¹H NMR spectrum of Fc[6]CPP in CDCl₃ (300 MHz).



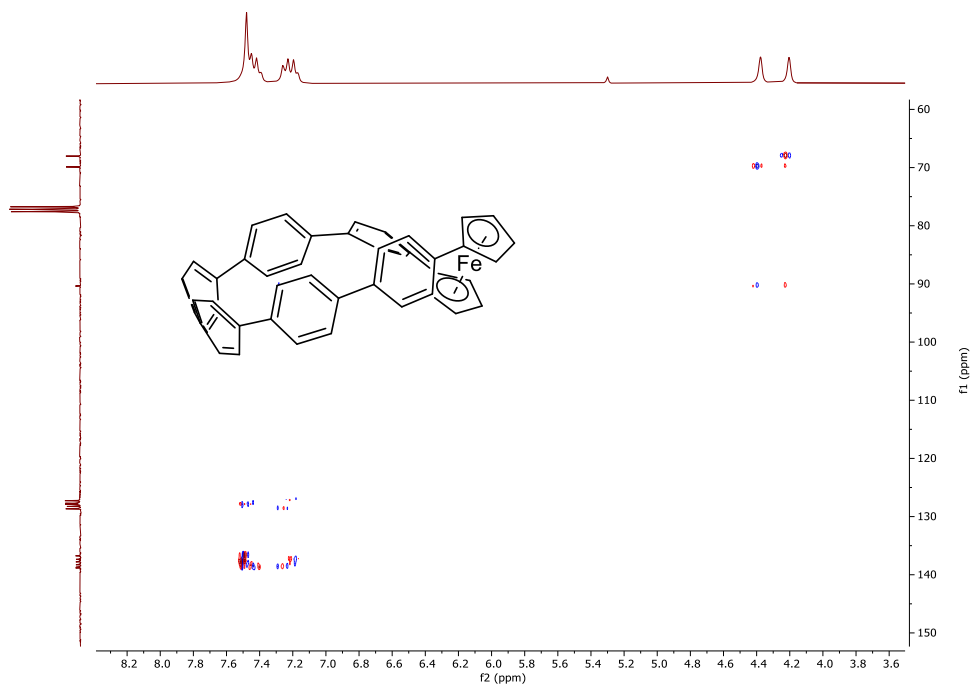
¹³C NMR spectrum of Fc[6]CPP in CDCl₃ (75 MHz).



^1H - ^1H COSY spectrum of **Fc[6]CPP** in CDCl_3 (300 MHz).

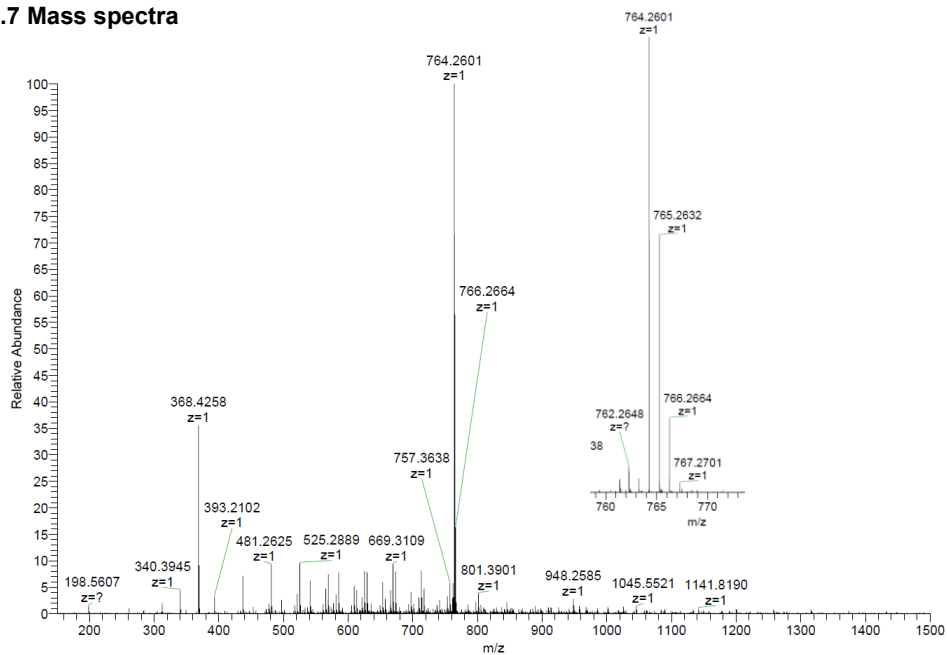


^1H - ^{13}C HSQC spectrum of **Fc[6]CPP** in CDCl_3 (300/75 MHz).

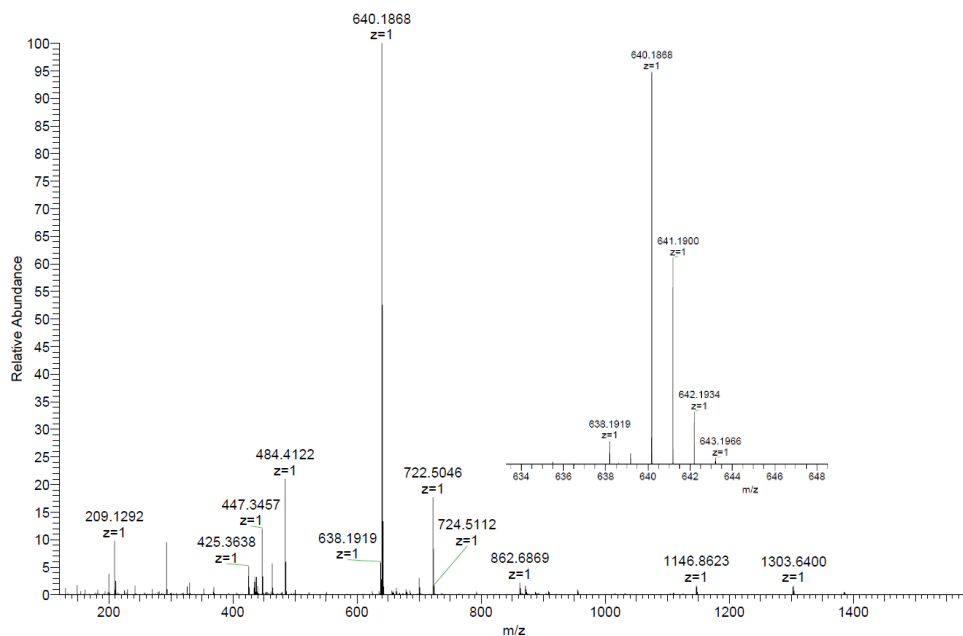


^1H - ^{13}C HMBC spectrum of **Fc[6]CPP** in CDCl_3 (300/75 MHz).

3.4.7 Mass spectra



HRMS spectrum of **pro-Fc[6]CPP** (NSI pos. EtOAc).



HRMS spectrum of Fc[6]CPP (NSI pos. EtOAc).

3.5 References

- [1] W. A. Eaton, E. R. Henry, J. Hofrichter, A. Mozzarelli, *Nat. Struct. Biol.* **1999**, *6*, 351–358.
- [2] P. Aisen, C. Enns, M. Wessling-Resnick, *Int. J. Biochem. Cell Biol.* **2001**, *33*, 940–959.
- [3] J. Liu, S. Chakraborty, P. Hosseinzadeh, Y. Yu, S. Tian, I. Petrik, A. Bhagi, Y. Lu, *Chem. Rev.* **2014**, *114*, 4366–4469.
- [4] P. Nordlund, P. Reichard, *Annu. Rev. Biochem.* **2006**, *75*, 681–706.
- [5] A. Nandi, L.-J. Yan, C. K. Jana, N. Das, *Oxid. Med. Cell. Longev.* **2019**, *2019*, 9613090.
- [6] D. Galaris, A. Barbouti, K. Pantopoulos, *Biochim. Biophys. Acta Mol. Cell Res.* **2019**, *1866*, 118535.
- [7] E. G. Kovaleva, J. D. Lipscomb, *Nat. Chem. Biol.* **2008**, *4*, 186–193.
- [8] T. A. Rouault, *Nat. Rev. Neurosci.* **2013**, *14*, 551–564.
- [9] J. Kim, M. Wessling-Resnick, *J. Nutr. Biochem.* **2014**, *25*, 1101–1107.
- [10] I. De Domenico, D. McVey Ward, J. Kaplan, *Nat. Rev. Mol. Cell Biol.* **2008**, *9*, 72–81.
- [11] M. Wessling-Resnick, *Annu. Rev. Nutr.* **2010**, *30*, 105–122.
- [12] O. Marques, G. Weiss, M. U. Muckenthaler, *Blood* **2022**, *140*, 2011–2023.
- [13] A. Pietrangelo, C. Trautwein, *Nat. Clin. Pract. Gastroenterol. Hepatol.* **2004**, *1*, 39–45.
- [14] G. Wilkinson, M. Rosenblum, M. C. Whiting, R. B. Woodward, *J. Am. Chem. Soc.* **1952**, *74*, 2125–2126.
- [15] K. E. Lewis, G. P. Smith, *J. Am. Chem. Soc.* **1984**, *106*, 4650–4651.

- [16] M. Tanabe, G. W. M. Vandermeulen, W. Y. Chan, P. W. Cyr, L. Vanderark, D. A. Rider, I. Manners, *Nat. Mater.* **2006**, *5*, 467–470.
- [17] R. L. N. Hailes, A. M. Oliver, J. Gwyther, G. R. Whittell, I. Manners, *Chem. Soc. Rev.* **2016**, *45*, 5358–5407.
- [18] D. Astruc, C. Ornelas, J. Ruiz Aranzaes, *J. Inorg. Organomet. Polym. Mater.* **2008**, *18*, 4–17.
- [19] R. Sun, L. Wang, H. Yu, Z.-Abdin, Y. Chen, J. Huang, R. Tong, *Organometallics* **2014**, *33*, 4560–4573.
- [20] O. Bernardo, S. González-Pelayo, L. A. López, *Eur. J. Inorg. Chem.* **2022**, *2022*, e202100911.
- [21] U. Rauf, G. Shabir, S. Bukhari, F. Albericio, A. Saeed, *Molecules* **2023**, *28*, 5765.
- [22] G. Roy, R. Gupta, S. Ranjan Sahoo, S. Saha, D. Asthana, P. Chandra Mondal, *Coord. Chem. Rev.* **2022**, *473*, 214816.
- [23] T. Mizuta, M. Onishi, K. Miyoshi, *Organometallics* **2000**, *19*, 5005–5009.
- [24] M. Tanabe, I. Manners, *J. Am. Chem. Soc.* **2004**, *126*, 11434–11435.
- [25] N. S. Jeong, W. Y. Chan, A. J. Lough, M. F. Haddow, I. Manners, *Chem. Weinh. Bergstr. Ger.* **2008**, *14*, 1253–1263.
- [26] D. E. Herbert, U. F. J. Mayer, J. B. Gilroy, M. J. López-Gómez, A. J. Lough, J. P. H. Charmant, I. Manners, *Chem. – Eur. J.* **2009**, *15*, 12234–12246.
- [27] S. K. Patra, G. R. Whittell, S. Nagiah, C.-L. Ho, W.-Y. Wong, I. Manners, *Chem. – Eur. J.* **2010**, *16*, 3240–3250.
- [28] M. Di Giannantonio, M. A. Ayer, E. Verde-Sesto, M. Lattuada, C. Weder, K. M. Fromm, *Angew. Chem. Int. Ed.* **2018**, *57*, 11445–11450.
- [29] Y. Sha, Y. Zhang, E. Xu, Z. Wang, T. Zhu, S. L. Craig, C. Tang, *ACS Macro Lett.* **2018**, *7*, 1174–1179.
- [30] Y. Zhang, Z. Wang, T. B. Kouznetsova, Y. Sha, E. Xu, L. Shannahan, M. Fermen-Coker, Y. Lin, C. Tang, S. L. Craig, *Nat. Chem.* **2021**, *13*, 56–62.
- [31] R. Jasti, J. Bhattacharjee, J. B. Neaton, C. R. Bertozzi, *J. Am. Chem. Soc.* **2008**, *130*, 17646–17647.
- [32] Y. Segawa, A. Yagi, K. Matsui, K. Itami, *Angew. Chem. Int. Ed.* **2016**, *55*, 5136–5158.
- [33] B. Lan, J. Xu, L. Zhu, X. Chen, H. Kono, P. Wang, X. Zuo, J. Yan, A. Yagi, Y. Zheng, S. Chen, Y. Yuan, K. Itami, Y. Li, *Precis. Chem.* **2024**, DOI 10.1021/prechem.3c00121.
- [34] L. Zhu, J. Xu, B. Lan, X. Chen, H. Kono, H. Xu, J. Yan, W. Li, A. Yagi, Y. Yuan, K. Itami, Y. Li, *Org. Chem. Front.* **2024**, *11*, 5130–5137.
- [35] N. Kubota, Y. Segawa, K. Itami, *J. Am. Chem. Soc.* **2015**, *137*, 1356–1361.
- [36] E. Kayahara, V. K. Patel, A. Mercier, E. P. Kündig, S. Yamago, *Angew. Chem. Int. Ed.* **2016**, *55*, 302–306.
- [37] J. M. Van Raden, S. Louie, L. N. Zakharov, R. Jasti, *J. Am. Chem. Soc.* **2017**, *139*, 2936–2939.
- [38] M. J. H. Ojea, J. M. V. Raden, S. Louie, R. Collins, D. Pividori, J. Cirera, K. Meyer, R. Jasti, R. A. Layfield, *Angew. Chem. Int. Ed.* **2021**, *60*, 3515–3518.
- [39] E. R. Darzi, B. M. White, L. K. Loventhal, L. N. Zakharov, R. Jasti, *J. Am. Chem. Soc.* **2017**, *139*, 3106–3114.
- [40] V. K. Patel, E. Kayahara, S. Yamago, *Chem. – Eur. J.* **2015**, *21*, 5742–5749.
- [41] T. C. Lovell, C. E. Colwell, L. N. Zakharov, R. Jasti, *Chem. Sci.* **2019**, *10*, 3786–3790.
- [42] P. Li, T. J. Sisto, E. R. Darzi, R. Jasti, *Org. Lett.* **2014**, *16*, 182–185.
- [43] P. J. Evans, L. N. Zakharov, R. Jasti, *J. Photochem. Photobiol. Chem.* **2019**, *382*, 111878.

- [44] J. D. Dunitz, L. E. Orgel, A. Rich, *Acta Crystallogr.* **1956**, *9*, 373–375.
- [45] Y. Segawa, H. Omachi, K. Itami, *Org. Lett.* **2010**, *12*, 2262–2265.
- [46] D. A. Foucher, B. Z. Tang, I. Manners, *J. Am. Chem. Soc.* **1992**, *114*, 6246–6248.
- [47] R. Rulkens, D. P. Gates, D. Balaishis, J. K. Pudelski, D. F. McIntosh, A. J. Lough, I. Manners, *J. Am. Chem. Soc.* **1997**, *119*, 10976–10986.
- [48] E. Khozeimeh Sarbisheh, H. Bhattacharjee, M. P. T. Cao, J. Zhu, J. Müller, *Organometallics* **2017**, *36*, 614–621.
- [49] M. S. Erickson, F. R. Fronczek, M. L. McLaughlin, *Tetrahedron Lett.* **1993**, *34*, 197–198.
- [50] J. K. Pudelski, M. R. Callstrom, *Organometallics* **1994**, *13*, 3095–3109.
- [51] K. R. Gordon, K. D. Warren, *Inorg. Chem.* **1978**, *17*, 987–994.
- [52] Y. Yamaguchi, W. Ding, C. T. Sanderson, M. L. Borden, M. J. Morgan, C. Kutal, *Coord. Chem. Rev.* **2007**, *251*, 515–524.
- [53] S. Scuppa, L. Orian, D. Dini, S. Santi, M. Meneghetti, *J. Phys. Chem. A* **2009**, *113*, 9286–9294.
- [54] S. Barlow, M. J. Drewitt, T. Dijkstra, J. C. Green, D. O'Hare, C. Whittingham, H. H. Wynn, D. P. Gates, I. Manners, J. M. Nelson, J. K. Pudelski, *Organometallics* **1998**, *17*, 2113–2120.
- [55] T. Mizuta, Y. Imamura, K. Miyoshi, H. Yorimitsu, K. Oshima, *Organometallics* **2005**, *24*, 990–996.
- [56] Y. Imamura, K. Kubo, T. Mizuta, K. Miyoshi, *Organometallics* **2006**, *25*, 2301–2307.
- [57] D. E. Herbert, M. Tanabe, S. C. Bourke, A. J. Lough, I. Manners, *J. Am. Chem. Soc.* **2008**, *130*, 4166–4176.
- [58] T. Mizuta, Y. Imamura, K. Miyoshi, *J. Am. Chem. Soc.* **2003**, *125*, 2068–2069.
- [59] W. Y. Chan, A. J. Lough, I. Manners, *Angew. Chem. Int. Ed.* **2007**, *46*, 9069–9072.
- [60] D. E. Herbert, J. B. Gilroy, W. Y. Chan, L. Chabanne, A. Staubitz, A. J. Lough, I. Manners, *J. Am. Chem. Soc.* **2009**, *131*, 14958–14968.
- [61] M. Kleoff, J. Schwan, L. Boeser, B. Hartmayer, M. Christmann, B. Sarkar, P. Heretsch, *Org. Lett.* **2020**, *22*, 902–907.
- [62] T. J. Sisto, M. R. Golder, E. S. Hirst, R. Jasti, *J. Am. Chem. Soc.* **2011**, *133*, 15800–15802.
- [63] Bruker, SAINT V8.40B, Bruker AXS Inc., Madison, Wisconsin, USA, **2001**.
- [64] L. Krause, R. Herbst-Irmer, G. M. Sheldrick, D. Stalke, *J. Appl. Crystallogr.* **2015**, *48*, 3–10.
- [65] G. M. Sheldrick, *Acta Crystallogr. Sect. Found. Adv.* **2015**, *71*, 3–8.
- [66] A. L. Spek, *Acta Crystallogr. Sect. C Struct. Chem.* **2015**, *71*, 9–18.
- [67] A. L. Spek, *J. Appl. Crystallogr.* **2003**, *36*, 7–13.
- [68] G. M. Sheldrick, *Acta Crystallogr. Sect. C Struct. Chem.* **2015**, *71*, 3–8.
- [69] Y. H. Hong, J. W. Han, J. Jung, T. Nakagawa, Y.-M. Lee, W. Nam, S. Fukuzumi, *J. Am. Chem. Soc.* **2019**, *141*, 9155–9159.
- [70] S. Witzel, M. Hoffmann, M. Rudolph, F. Rominger, A. Dreuw, A. S. K. Hashmi, *Adv. Synth. Catal.* **2022**, *364*, 581–592.
- [71] *Welcome to Prizmatix.com*. <https://www.prizmatix.com/index.html> (accessed 2024-08-06).
- [72] *Photo Sciences Publications | Kessil LED*. Kessil. https://www.Kessil.com/products/science_publications.php (accessed 2024-08-06).
- [73] M. J. Frisch, G. W. Trucks, H. B. Schlegel, G. E. Scuseria, M. A. Robb, J. R. Cheeseman, G. Scalmani, V. Barone, G. A. Petersson, H. Nakatsuji, X. Li, M. Caricato, A. V. Marenich,

J. Bloino, B. G. Janesko, R. Gomperts, B. Mennucci, H. P. Hratchian, J. V. Ortiz, A. F. Izmaylov, J. L. Sonnenberg, Williams, F. Ding, F. Lipparini, F. Egidi, J. Goings, B. Peng, A. Petrone, T. Henderson, D. Ranasinghe, V. G. Zakrzewski, J. Gao, N. Rega, G. Zheng, W. Liang, M. Hada, M. Ehara, K. Toyota, R. Fukuda, J. Hasegawa, M. Ishida, T. Nakajima, Y. Honda, O. Kitao, H. Nakai, T. Vreven, K. Throssell, J. A. Montgomery Jr., J. E. Peralta, F. Ogliaro, M. J. Bearpark, J. J. Heyd, E. N. Brothers, K. N. Kudin, V. N. Staroverov, T. A. Keith, R. Kobayashi, J. Normand, K. Raghavachari, A. P. Rendell, J. C. Burant, S. S. Iyengar, J. Tomasi, M. Cossi, J. M. Millam, M. Klene, C. Adamo, R. Cammi, J. W. Ochterski, R. L. Martin, K. Morokuma, O. Farkas, J. B. Foresman, D. J. Fox, **2016**.